



A 3D analytical model for orthogonal blade-vortex interaction noise



Michael E. Quaglia^{a,*}, Thomas Léonard^a, Stéphane Moreau^a, Michel Roger^b

^a University of Sherbrooke, 2500 bd de l'université, J1K 2R1 Sherbrooke, QC, Canada

^b École Centrale de Lyon, 36 Avenue Guy de Collongue, 69134 Écully, France

ARTICLE INFO

Article history:

Received 16 November 2016

Received in revised form

21 March 2017

Accepted 23 March 2017

Handling Editor: A.V. Metrikine

Available online 12 April 2017

Keywords:

Counter-Rotating Open Rotor noise

Blade-Vortex Interaction

Tonal noise

Turbomachinery

Analytical method

ABSTRACT

A 3D analytical model of an Orthogonal Blade-Vortex Interaction (OBVI) for Counter-Rotating Open Rotor (CROR) tonal noise is investigated. The specific influence of two parameters taking into account the three-dimensionality of both the vortex velocity and the convection velocity within the rotor-rotor volume is addressed. The first step is to extract the vortex parameters from a recent unsteady Reynolds-Averaged Navier-Stokes computation and validate different vortex models. Lamb-Oseen and Scully vortices reproduce the behavior of the tip-vortex tangential velocity fairly well. Regarding the vortex axial velocity modeling, a Gaussian profile fits well with numerical results. On the one hand, the impact of the stream-tube contraction unbalances the lobes of the unsteady pressure with opposite phases produced by the OBVI event. This effect is larger than that of an equivalent blade sweep. On the other hand, adding the axial velocity deficit to the tangential one also unbalances the pressure lobes. Finally, from an acoustic point of view using Curle's acoustic analogy, both the stream-tube contraction and the axial velocity deficit have the same effect: they turn an acoustically-low efficient quadrupole into a strong dipole making these parameters fundamental for future CROR OBVI investigations.

© 2017 Elsevier Ltd. All rights reserved.

1. Introduction

Because of the weight and space limitations of nacelles for future Ultra High By-Pass Ratio (UHBR) turbofans, Counter-Rotating Open Rotor (CROR) design could be a viable alternative to classical turboengines for commercial airplane propulsion. Since the beginning of CROR design with the preliminary work on the UnDucted Fan engine in the nineties [1–5], significant tonal noise reduction for this novel architecture has been achieved. Nowadays, 3D aerodynamic and aeroacoustic optimizations have yielded fully three-dimensional blade shapes and cropped aft rotor that have achieved substantial reductions in tonal noise without efficiency penalties at cruise conditions [6]. Yet, one of the main concerns regarding CROR noise, is to meet the community noise levels standards set by the International Civil Aviation Organization at take-off and approach conditions. At these regimes, it is particularly essential to take into account the three-dimensionality of the flow induced by unbalanced flow conditions within the CROR due to inflow incidence or streamtube contraction between the front and rear rotors. At these flow regimes, cropping the aft rotor might be insufficient to reduce the interaction noise due to the front-rotor tip vortex impingement as was recently shown by Soulat et al. [7]. In a typical uncropped CROR

* Corresponding author.

E-mail addresses: michael.quaglia@usherbrooke.ca (M.E. Quaglia), thomas.leonard@usherbrooke.ca (T. Léonard), stephane.moreau@usherbrooke.ca (S. Moreau), michel.roger@ec-lyon.fr (M. Roger).

Nomenclature*Latin symbols*

| | |
|---------------------------|---|
| a, b | constants in the Lamb-Oseen gust spectrum |
| a_ν | constant in the turbulent kinematic viscosity |
| V_z^{max} | maximum of the vortex axial velocity |
| r_0 | radius of the vortex core |
| k | acoustic wavenumber |
| b_φ, Φ_i | coefficients of the helix regression in the azimuthal direction |
| c | chord length |
| $R1(R2)$ | front (aft) - rotor |
| R_{V1} | radius of the OBVI event |
| $C_{chord}(C_{span})$ | amplitude of the projection angle related to the chordwise (spanwise) variable |
| C_{amp} | amplitude of the upwashes spectral density |
| \bar{p} | aerodynamic surface pressure on the blade |
| \bar{l}_{tot} | total aerodynamic pressure jump on the blade |
| \tilde{G}^* | upwash spectral density related to the azimuthal velocity of the vortex |
| \tilde{G}^{z_v} | upwash spectral density related to the axial velocity of the vortex |
| \tilde{G}^{tot} | upwash spectral density related to all velocities. |
| \mathbf{U}_0 | convection velocity vector |
| c_β | vena contracta contraction radius coefficient |
| S_0 | source-observer distance corrected by 1D convection velocity |
| R | Observer radius of the microphone |
| V_θ^{max} | $\sqrt{x_{c2}^2 + y_{c2}^2 + z_{c2}^2}$ maximum of the vortex azimuthal velocity |
| U_c | phase speed of the incoming vortex] |
| w | upwash velocity |
| (X_v, Y_v, Z_v) | coordinates of the vortex core line |
| r_X | viscous vortex radius growth rate |
| r_i | initial viscous vortex radius value |
| V_X^{max} | viscous azimuthal-vortex maximum velocity |
| | diffusion rate |
| V_i^{max} | initial viscous azimuthal-vortex maximum velocity value |
| p_{atm} | standard atmospheric pressure (101325 Pa.) |
| (u_v, v_v, z_v) | vortex velocity in the vortex reference frame |
| (u_v, v_β, z_β) | vortex velocity in the vortex-vena contracta corrected reference frame |
| (k_x, k_y, k_z) | aerodynamic wavenumbers in the unswept |

blade reference frame

| | |
|----------------------------|--|
| (r_v, θ_v, z_v) | vortex reference frame in cylindrical coordinates |
| (x_{c2}, y_{c2}, z_{c2}) | unswept aft-blade reference frame in Cartesian coordinates |
| (X, Y, Z) | global reference frame in Cartesian coordinates |
| (X, R^c, Φ) | global reference frame in cylindrical coordinates |
| $(R_{V1}\Phi), R_{V1}, X)$ | unwrapped OBVI reference frame in Cartesian coordinates |

Greek symbols

| | |
|----------------------|---|
| a_β, R_i | coefficients of the helix regression in the radial direction |
| Γ | total circulation of the vortex |
| φ | helicity angle of the vortex trajectory |
| $\gamma_1(\gamma_2)$ | front (aft) rotor stagger angle at the OBVI location |
| β | Vena contracta angle |
| $\beta_1(\beta_2)$ | compressibility coefficient in the chordwise (spanwise) direction |
| κ | Helmholtz parameter |
| α | Lamb-Oseen maximum velocity location coefficient |
| Φ' | dimensionless velocity potential |
| $\nu(\nu_t)$ | Laminar (turbulent) kinematic viscosity |
| ρ_0 | density of the flow at rest |

Subscripts/Superscripts

| | |
|--------------------|--|
| $(\cdot)^{LO}$ | variable related to the Lamb-Oseen vortex model |
| $(\cdot)^{Sc}$ | variable related to the Scully vortex model |
| $(\cdot)^{Va}$ | variable related to the Vatisas vortex model |
| $(\cdot)^{LE}$ | variable related to the first iteration of the Amiet-Schwarzschild method |
| $(\cdot)^{TE}$ | variable related to the second iteration of the Amiet-Schwarzschild method |
| $(\cdot)'$ | variable in the cartesian swept coordinate system |
| $(\cdot)^*$ | Dimensionless coordinate |
| $(\cdot), (\cdot)$ | variable in the Fourier space |

configuration computed at cruise and take-off conditions, Peters and Spakovszky [8] showed numerically that the tip contribution caused by the Orthogonal Blade-Vortex Interaction (OBVI) can be as large as the front rotor-wake impact for specific interaction frequencies. It is then essential to assess tonal noise for this case with accurate but quick model of the OBVI noise mechanism. An analytical procedure was recently proposed by Roger et al. [9] to predict OBVI tonal noise for CROR preliminary designs. The present work extends the aforementioned model by introducing two new features.

The first one takes into account the fact that the streamtube for an open-rotor at approach contracts inwardly. This effect, called stream-tube contraction, is seen both in numerical simulations [10,11] and experiments [12]. The contraction is taken into account using an additional angle thereafter called β . A single angle is used because Computational Fluid Dynamics (CFD) results exhibit such variations when tracking the vorticity maximum in the tip region between the two rotors (Fig. 1 in [13]). For CROR designs, a linear approach is more realistic than the rational-linear regression based on single rotor experiments [12].

The second feature is to provide a truly 3D vortex model by adding an axial velocity on top of the tangential velocity used

previously by Roger et al. [9]. Both components are essential in order to investigate CROR OBVI because of the helical path of the blade wakes. Both velocities have the same order of magnitude showing that the tip-vortex is a complete 3D pattern. Moreover, similarly to what was previously shown [14–16], the axial velocity is a “wake-like” contribution following the description given by Fabre [17].

The paper is split into three main parts similarly to the preliminary investigation performed by Quaglia et al [13]. First, the global methodology used in the analytical model is provided. Secondly the results of the model are computed at each step of the methodology and compared with numerical extractions. Finally some conclusions are drawn about the two parameters investigated.

2. Methodology

The OBVI model is based on the linearized theory of the response of a thin flat-plate to incoming velocity fluctuations or gusts. The problem is formulated in the frequency domain as the OBVI is periodic and can be seen as harmonic variations of the angle of attack around a zero mean loading induced by the incoming upwash velocity. Vortex stretching and deformation induced by the chopping of the aft blade are thus ignored. This assumption is made because CROR blades are thin and slightly cambered. The vortex is described by different analytical models that are simple enough and physically consistent. Contrary to Roger et al. [9] where the blade was ultimately assumed to have a finite span, the present paper only shows infinite span results. Once the unsteady pressure jump is obtained, an acoustic analogy is used to yield the far-field noise. In order to provide a clear insight into the influence of the additional parameters on the generated sound, Curle’s acoustic analogy is applied to a fixed rectangular flat blade. Later on the OBVI is based on the strip theory where the propeller blades are split into thin annuli. The unsteady aerodynamics of a blade segment is determined as if it was in translation tangent to the real helical motion. Flow conditions are thus homogeneous in both streamwise and spanwise directions. Fig. 1 summarizes the different steps of the complete model:

- I. Modeling the tip vortex using classical 2D or 3D analytical models [18–20].
- II. Projecting the vortex velocities within the moving aft blade reference frame in order to compute the upwashes.
- III. Computing the unsteady lift induced by these upwashes using 2D linearized thin-airfoil theories [21,22,9].
- IV. Computing the tonal noise using Curle’s acoustic analogy [23].

The methodology also implies several projections or changes of Reference Frames (RF). First, step I starts from the global RF (X, Y, Z) or (R^c, ϕ, X) in cylindrical coordinates where the X direction is aligned with the rotational axis of the CROR pointing downstream (Fig. 2(a)). In this RF, the vortex path centerline (X_v, Y_v, Z_v) is extracted from CFD results. Using this moving RF center, the vortex velocities are extracted in the local vortex RF (r_v, θ_v, z_v) using cylindrical coordinates usual for vortex motion descriptions. Afterward, step II projects the vortex velocities described in the vortex local RF to the unswept aft-blade RF. The associated RF rotations are described in Table 1. The origin of the rotations are taken at the impingement locus between the vortex centerline and the leading edge of the aft blade $\vec{O}_{v1} = (R_{v1}, \phi_{v1}, X_{v1})$. Fig. 2(b) shows the new intermediate RF introduced between the vortex local cartesian RF (u_v, v_v, z_v) and the unwrapped coordinate RF in order to take into account the stream-tube contraction angle (β) in the cutting process ($u_\beta, v_\beta, z_\beta$). Fig. 2(c) shows that the helicity of the vortex path (φ) and the aft blade stagger (χ_2) are also used to extract the velocity fluctuations impinging on the unswept blade (y_{c2}, z_{c2}, x_{c2}). Note that the z_{c2} axis coincides with the v_β axis. Finally, steps III and IV are computed in the aft-blade RF (y_{c2}, z'_{c2}, x'_{c2}) presented in Fig. 2(d) taking into account the sweep angle (Ψ).

The geometrical features of the OBVI event are obtained based on a modern CROR geometry at approach condition that has been extensively studied with Unsteady Reynolds-Averaged Navier-Stokes (URANS) simulations [24,10]. The latter was performed on a 5 million grid point multi-block structured grid using the cell-centered turbomachinery solver Turb’Flow

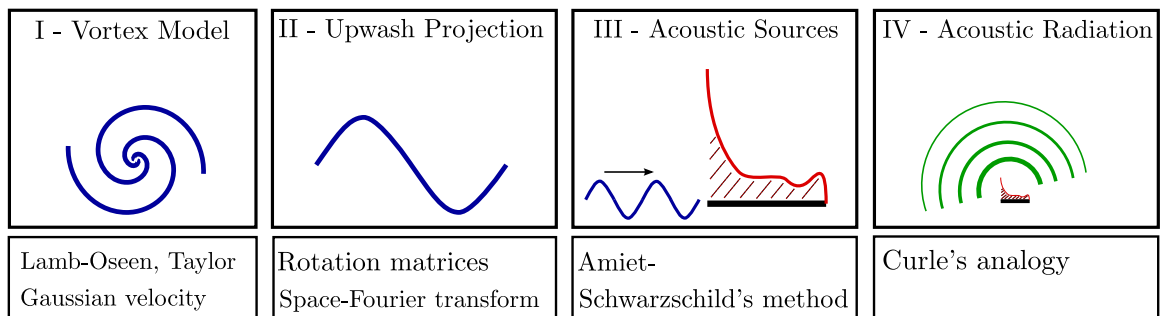


Fig. 1. Orthogonal Blade-Vortex Interaction model breakdown.

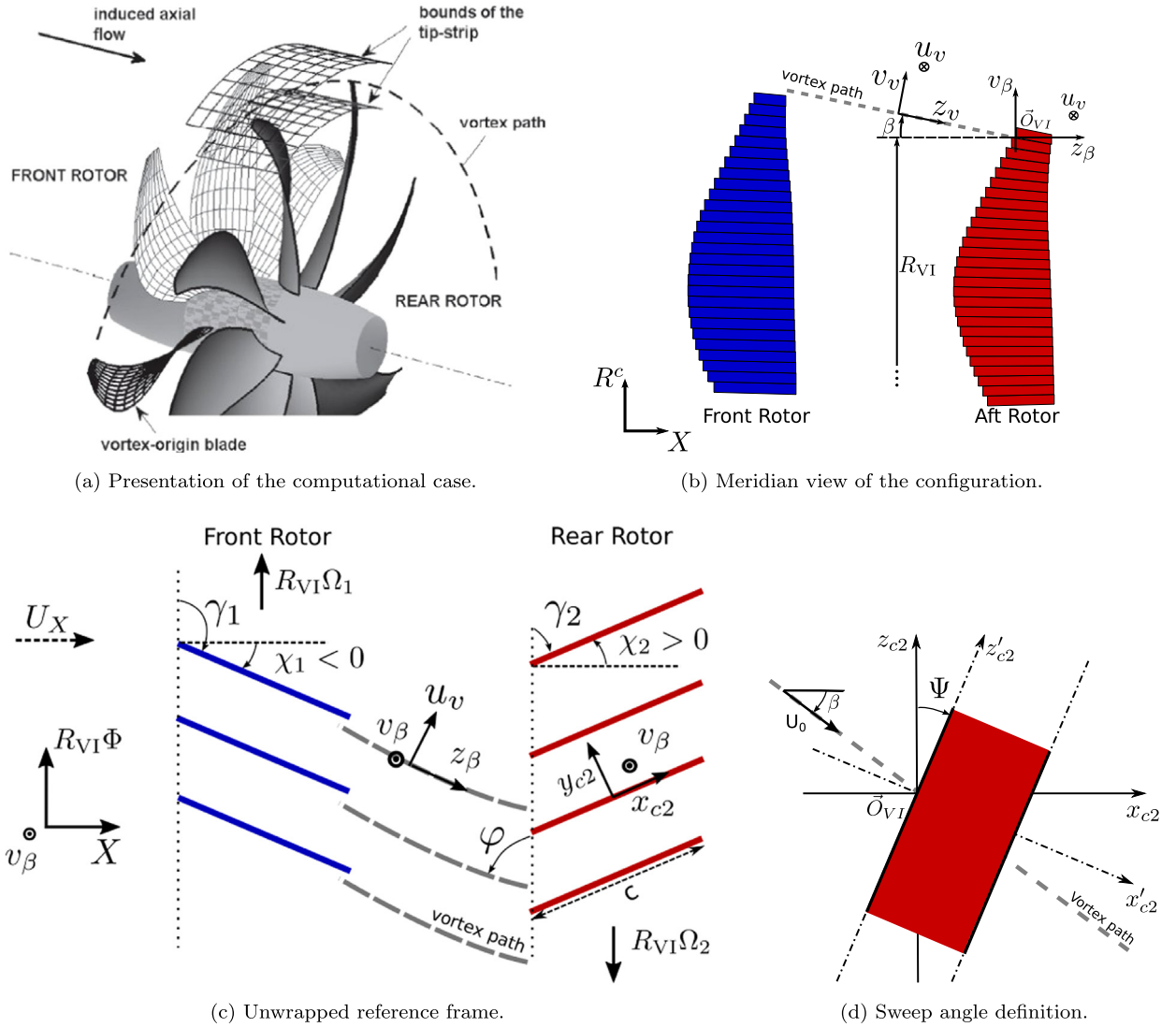


Fig. 2. Presentation of the reference frames, based on Roger et al. [9].

Table 1

Description of the different reference frames for the upwash computation. The origin of all rotation matrices is $\vec{O}_{VI} = (R_{VI}, \Phi_{VI}, X_{VI})$ described in the cylindrical global RF. Direct permutation of the coordinates was used in order to show the rotational axis.

| RF# | Rotational axis | angle RF#-1 | Ref coordinates |
|-----|-----------------|-------------|------------------------------|
| 1 | ~ | ~ | (r_v, θ_v, z_v) |
| 2 | $(0, 0, 1)$ | θ_v | (u_v, v_v, z_v) |
| 3 | $(1, 0, 0)$ | β | (u_v, v_β, z_β) |
| 4 | $(0, 1, 0)$ | φ | $(R_{VI}\Phi, v_\beta, X)$ |
| 5 | $(0, 1, 0)$ | χ_2 | (y_{c2}, z_{c2}, x_{c2}) |
| 6 | $(1, 0, 0)$ | ψ | $(y_{c2}, z'_{c2}, x'_{c2})$ |

developed at Ecole Centrale de Lyon [25]. A sliding mesh approach was used with an interface about half-way between the two rotors. Spatial discretization was achieved with the second-order upwind AUSM+–up scheme [26] and the Van Albada limiter for the conservative variables (density, momentum and energy), whereas a first-order upwind scheme was used for the turbulent flow field. Time discretization was achieved using an explicit second-order 5-steps Runge-Kutta scheme. Turbulence was modeled with Kok’s two equation $k-\omega$ model [27] coupled with Menter’s turbulence kinetic energy production limiter [28]. More details can be found in Soulat et al. [7]. The front rotor (called R1) has 12 blades whereas the aft-

rotor (called R2) has 10 blades. This configuration is close to the F31/A31 NASA geometry [29]. Using periodic boundary conditions, an equivalent 12x12 case is computed assuming a single channel computational domain. This case is defined to preserve the aerodynamic performances. In these conditions, the velocity fluctuations coming from the front rotor are assumed not to be modified by the aft-rotor blade number.

3. Vortex modeling results

The first step is to extract the streamline of the vortex core from its inception close to the tip of the front-rotor trailing edge to the leading edge of the aft-rotor. In order to detect the vortex center several search algorithms can be used [30]. In this work, a maximum vorticity method [31] was used in order to extract the streamline from the CFD domain because the vortex is convected outside the boundary layers. Other algorithms were tested with little differences seen in the final results. The extracted vortex core streamline was smoothed in order to remove the local instabilities related to its convection and rolling process [17]. A helix equation with a varying radius is used. It reads:

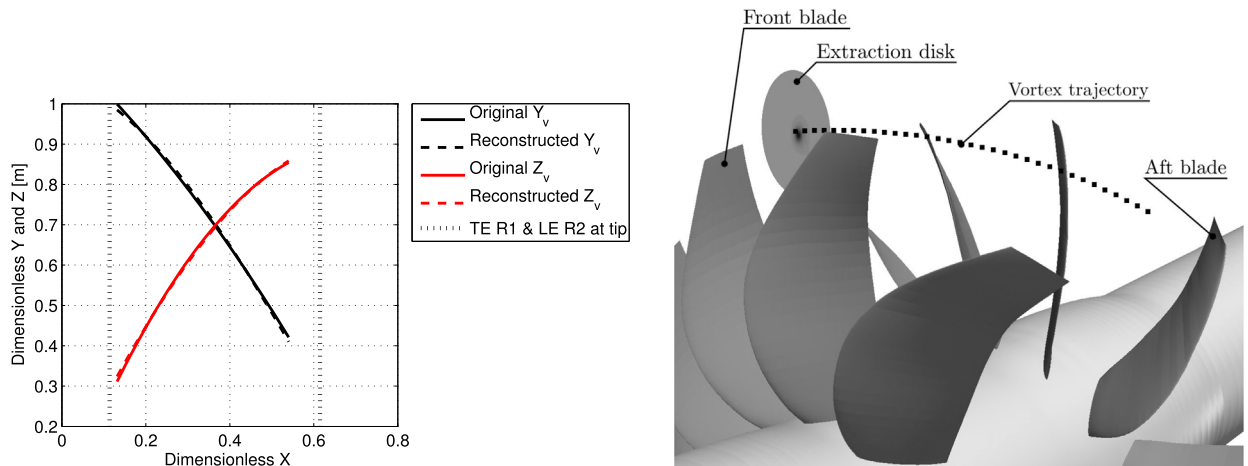
$$\begin{cases} Y_v(X_v) = R_v \cos(b_\varphi X_v + \Phi_i) \\ Z_v(X_v) = R_v \sin(b_\varphi X_v + \Phi_i) \end{cases} \quad (1)$$

where (X_v, Y_v, Z_v) stands for the vortex core streamline trajectory in Cartesian coordinates (X, Y, Z) , R_v is the radius in the cylindrical coordinates, b_φ is the axial advance of the helix and Φ_i is the angular origin of the helix. Because of the stream-tube contraction, R_v is modified along X_v . This effect is modeled by a linear variation of the vortex-core radius is used:

$$R_v(X_v) = a_\beta X_v + R_i \quad (2)$$

with a_β the coefficient related to the stream-tube contraction angle and R_i related to the initial radius of the helix. The linear regression was used over the classical linear-rational formulation [12] in view of CFD extractions and recent experimental extractions repeated on the F31/A31 geometry [32]. The smoothed streamline is used in order to simplify the extraction of the OBVI geometrical parameters. Fig. 3a shows the trajectory. It confirms the quality of the comparison of the smoothed streamline with direct CFD extractions. Hardly any difference can be seen on the trajectory thus the regression captures the behavior of the vortex core accurately.

From Fig. 3(b) the smoothed streamline (solid dots) is used to extract the relative vortex velocities in the local vortex reference frame (r_v, θ_v, z_v) using a disk locally normal to the trajectory and making the vortex center the local origin of the reference frame. Because the vortex is not purely axisymmetric, the azimuthal average is computed. However, Fig. 4 (a) shows that the disks coming from the CFD grid are not uniform in the vortex azimuthal direction (θ_v) , thus the results are interpolated on a grid uniform in azimuth presented in Fig. 4(b). The latter shows that the interpolation accurately captures the variations of the static pressure on the raw grid. The interpolated grid has a smaller radius compared with the raw grid in order to remove the values when the disk crosses the surface of the aft-blades. Extraction of the tangential and axial velocities is achieved in the same plane at 50% of the $R1 - R2$ distance. The azimuthal average of these velocity components and the standard deviation around it are shown in Fig. 5. The standard deviation remains small close to the vortex core, consistently with the pressure maps that show a well defined round vortex in Fig. 4, and grows away from the core where



(a) Extracted and reconstructed trajectories.

(b) Global view of the extraction procedure.

Fig. 3. The vortex extraction procedure, using the current CROR geometry presented by Soulat et al. [24], trajectories are made dimensionless by the front-rotor tip radius.

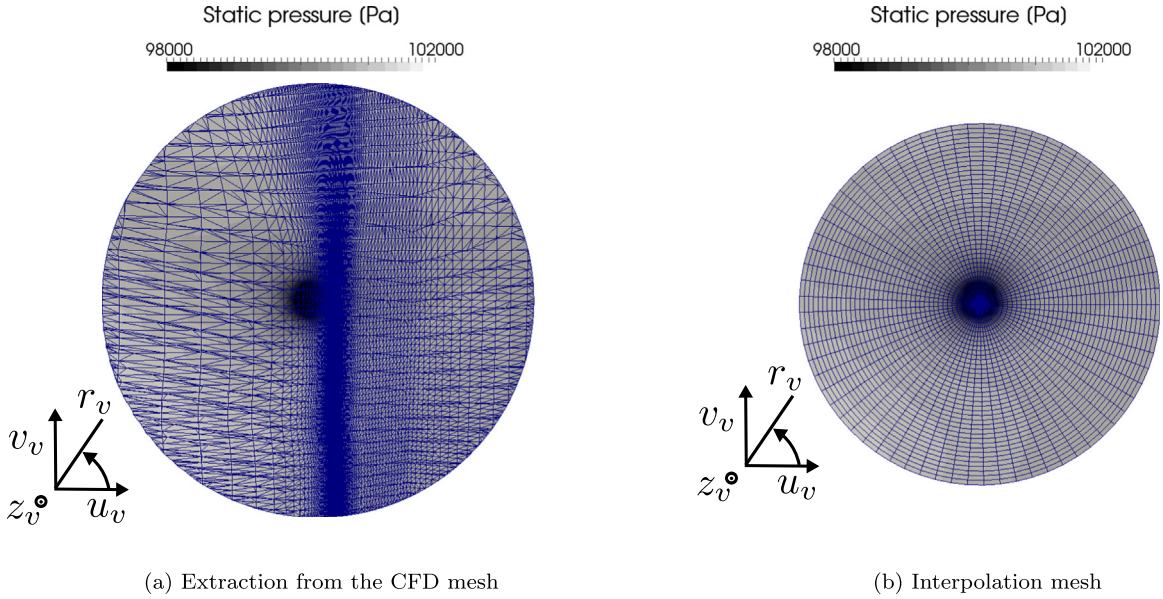


Fig. 4. Vortex static pressure extraction at 50% of the R1 – R2 distance.

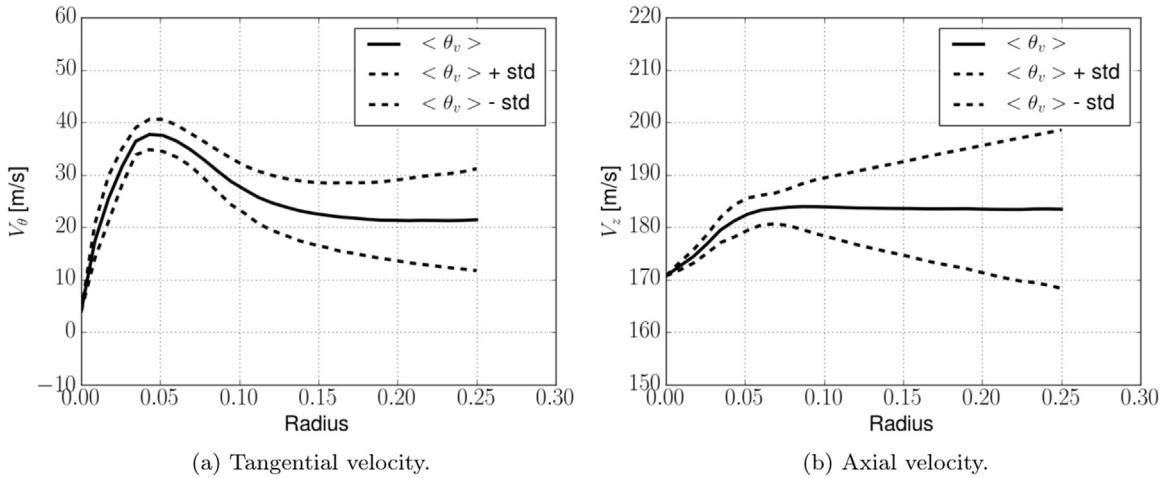


Fig. 5. Vortex velocity extractions at 50% of the R1 – R2 distance. Standard deviations around the azimuthal average of both tangential and axial velocities.

the non-uniform convection flow shears the vortex.

From this grid, the azimuthal average is computed for both the azimuthal and axial local velocities. Fig. 6 shows the result of the extractions for three different axial positions: one close to the front rotor trailing edge, one approximately at half distance between the front and aft rotors and one extracted as close as possible from the BVI event. All velocity profiles are made dimensionless by the front rotor tip velocity. Figs. 6(a) and (b) show that the vortex diffuses during its convection from the front to the rear rotor. The pressure deficit behavior (Fig. 6(c)) is related to a local radial equilibrium that can be seen in several other vortex extractions [15].

From the latest plane (85%R1 – R2 distance), the maximum azimuthal V_{θ}^{max} and axial V_z^{max} velocities are extracted together with the vortex core radius r_0 in the vortex RF (r_v, θ_v, z_v) to provide inputs for the analytical models. r_0 is also called the viscous radius and is defined as the radius where the azimuthal velocity reaches its maximum. The major difference between analytical models is the presence or the lack of total circulation Γ [20]:

$$\Gamma = \lim_{r \rightarrow \infty} \int_0^{2\pi} V_{\theta}(r) r dr d\theta. \tag{3}$$

Vortices with circulation are characterized by a low tangential velocity decay rate outside the vortex core. As the influence of the decay rate is a key parameter in BVI noise [33,15], three vortex models have been investigated:

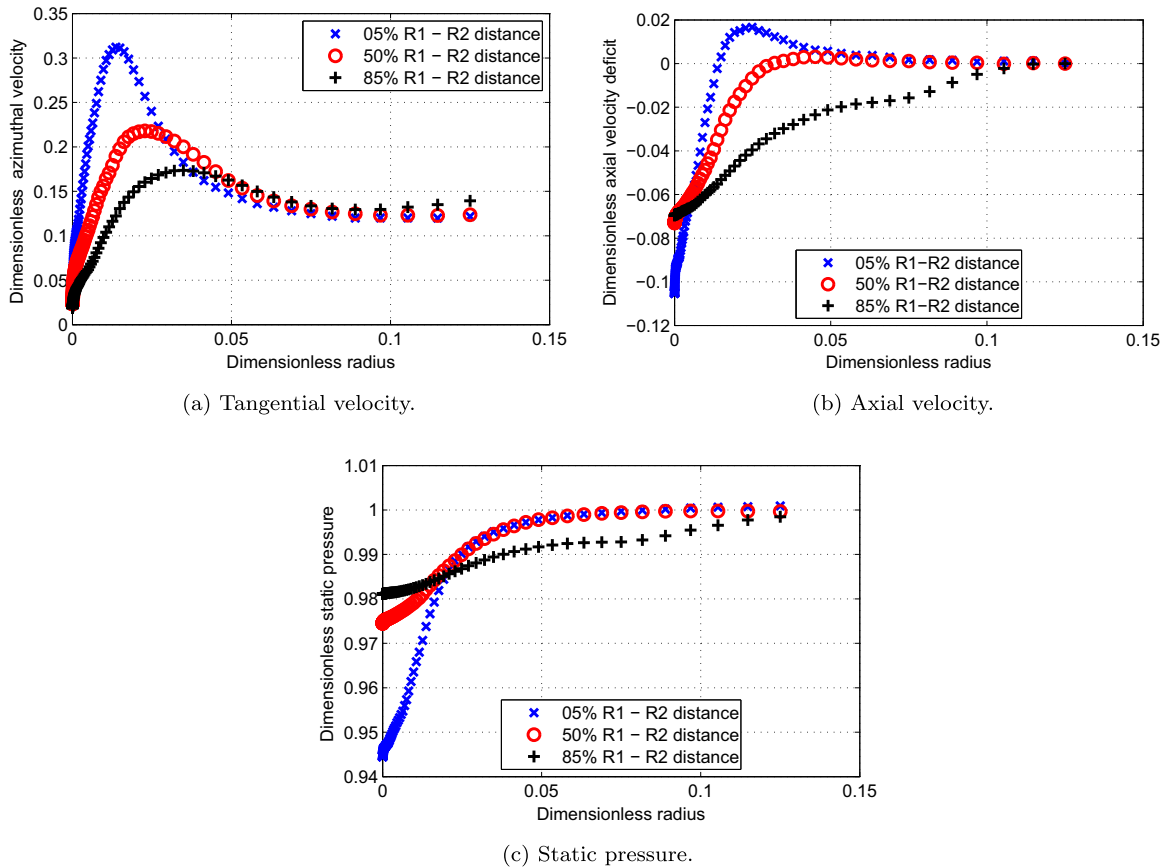


Fig. 6. Vortex extractions for different axial positions. Velocities, distances and pressure are respectively made dimensionless by the front rotor tip velocity, the front rotor radius and the atmospheric pressure.

1. The Lamb-Oseen vortex (LO) [18], a vortex with circulation that provides the baseline to compare with the previous results from Roger et al. [9].
2. The Scully vortex (Sc) [34], a vortex with circulation similar to the Lamb-Oseen that is meant to double check the modifications induced by the additional stream-tube contraction angle.
3. The Taylor vortex (Ta), a vortex without circulation, which is used to compare with vortices with circulation. This vortex is a particular case of the Carton-McWilliams shielded vortex family [20].

V_{θ}^{max} and r_0 are used in order to feed tangential velocity models. The tangential velocity formula of the aforementioned models are respectively:

$$V_{\theta}^{LO}(r) = \frac{V_{\theta}^{max} r_0}{r} \frac{1 - e^{-\alpha^2 (r/r_0)^2}}{1 - e^{-\alpha^2}}, \quad V_{\theta}^{Sc}(r) = \frac{2 V_{\theta}^{max} r}{r_0 ((r/r_0)^2 + 1)}, \quad V_{\theta}^{Ta}(r) = \frac{V_{\theta}^{max} r}{r_0} e^{\frac{1}{2}(1 - (r/r_0)^2)}, \quad (4)$$

where the coefficient $\alpha \approx 1.121$ is used in order to have the peak velocity at $r = r_0$ for the Lamb-Oseen vortex.

Fig. 7(a) shows the behavior of analytical models compared with CFD extractions. Discrepancies between the results are attributed to the convection velocity that is not purely normal to the extraction plane. The axial velocity was also considered since it was shown as fundamental in OBVI noise for CROR [35]. A classical Gaussian velocity deficit formulation has been used [17]:

$$V_z^{Gau}(r) = V_z^{max} \exp\left(-[r/r_0]^2\right). \quad (5)$$

Fig. 7(b) shows that this Gaussian velocity predicts the axial behavior of the vortex fairly well.

The advantage of analytical models such as Lamb-Oseen vortex is that they include diffusion. For Lamb-Oseen vortex model, such a diffusion comes from viscosity and the vortex core radius growth rate is [36]:

$$r_0^2(t) = 4(\nu + \nu_t)t, \quad (6)$$

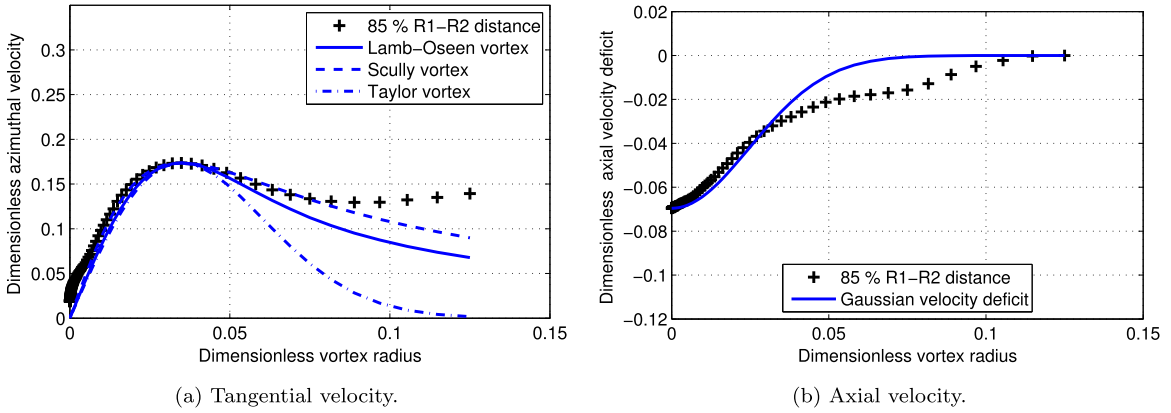


Fig. 7. Comparison of numerical and analytical tangential and axial velocities for the 85% extraction plane, in the vortex reference frame (r_v, θ_v, z_v) . Velocities are made dimensionless by the front rotor tip rotational velocity, distances are made dimensionless by the front rotor radius.

using ν the kinematic viscosity, $\nu_t = a_\nu \Gamma$ the turbulent viscosity and t the convection time since the inception of the vortex at the trailing edge of the blade. As Squire [36] mentioned, the turbulent velocity ν_t scales with the circulation of the vortex. In order to use the model with Reynolds-Averaged Navier-Stokes (RANS) mixing plane results where the knowledge of the vortex parameters are unknown at the OBVI location, extrapolation of V^{max} and r_0 parameters are performed assuming linear and inverse power regressions from r_0 and V^{max} parameters respectively:

$$\begin{cases} r_0^2(X^*) = r_X^2 X^* + r_i^2, \\ V^{max}(X^*) = \frac{V_X^{max}}{\sqrt{X^*}} + V_i^{max}, \end{cases} \quad (7)$$

where X^* indicates the dimensionless axial position of the vortex centerline. Fig. 8 show results using the aforementioned formulas. Only small discrepancies can be seen between URANS extraction and the regressions, showing that the viscous diffusion modeling works fairly well for a vortex convected with a helical motion and with a non-uniform convection velocity. Larger discrepancies can be seen for the regression using only the results from the R1 domain but these differences remain small enough to provide a realistic prediction from RANS simulations.

Finally to check the quality of the analytical model a recomposition of the radial velocity fluctuations from the analytical velocity is compared with CFD extractions in Fig. 7(a). The differences between the extractions and the analytical model come from the non-uniform convection velocity of the vortex as mentioned above in Fig. 5. Figs. 9(a) and (b) show that the analytical model captures fairly well the velocity fluctuations in the global reference frame only when a model with circulation is used. Note that despite the fact that the vortex motion is completely 3D, the radial velocity recomposition (Fig. 9) is made on an iso-radius line passing through the vortex core. By doing so only the tangential velocity is required in order to compare analytical values with numerical extractions.

Because Taylor vortex results poorly represent the current test case and because Scully and Lamb-Oseen vortices behave similarly [13], results for the analytical models are mostly showed for the Lamb-Oseen model coupled with the Gaussian axial velocity deficit. Yet the upwash velocities are derived for the 3 models in the next section.

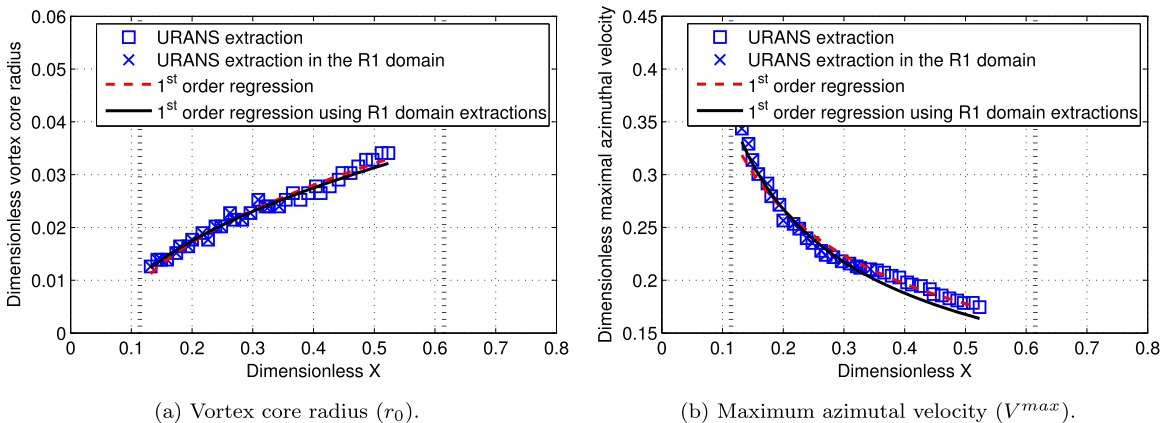


Fig. 8. Variations of the analytical vortex model parameters in the rotor-rotor volume.

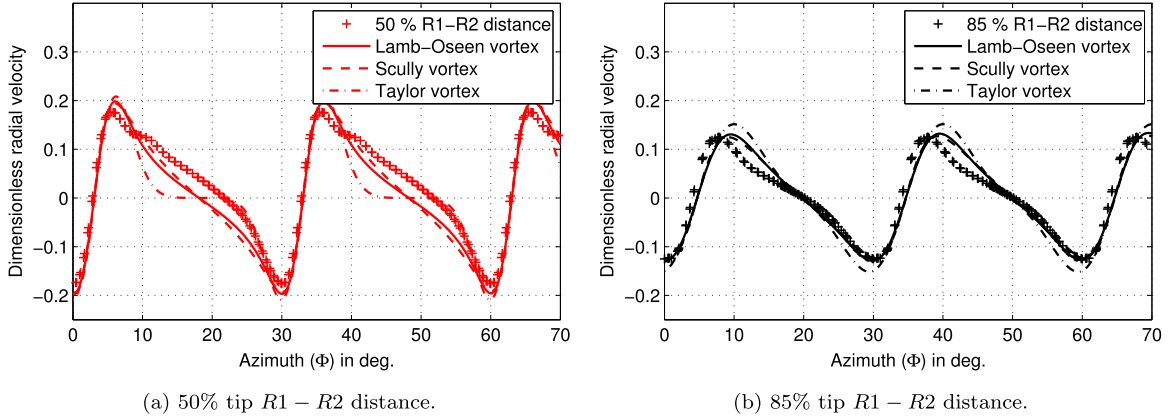


Fig. 9. Comparison of radial velocity between numerical extractions and the analytical models using the global reference frame (X, Y, Z).

4. Spectral upwash results

Having generalized the vortex model in 3D, the upwash velocity seen by the rear-rotor blade can be computed. The vortices shed by the front blades are convected to the aft blade tip region within the bounds of a *tip-strip*. Between the bounds of the tip-strip the convection velocity of the vortex is assumed constant. This means that the viscous radius of the vortex core is significantly smaller than the radius of a CROR blade ($R_{VI} \gg r_0$) in the straight vortex path introduced by Roger et al. [9] to avoid any possible confusion with the local radius of the spiral.

The upwashes are the velocity fluctuations in the y_{c2} direction for $y_{c2} = 0$. The stream-tube contraction angle β is introduced in an intermediate RF between the (u_v, v_v, z_v) and the $(X, R_{VI}, R_{VI}\Phi)$ RFs. The rotational axis is in the u_v direction because the vortex path is radially contracting in the R_{VI} direction. From the parameters of the helix regression described in Eq. (1), a_β is related to the stream-tube contraction angle and b_φ is related to the helicity of the vortex using the formulas:

$$\begin{cases} \beta = \text{atan}(a_\beta) \\ \varphi = \text{atan}\left(\frac{1}{b_\varphi R_{VI}}\right). \end{cases} \quad (8)$$

Using the Lamb-Oseen vortex, the analytical upwash is obtained as

$$w^{LO}(x_{c2}, 0, z_{c2}, t) = V_\theta^{LO}(r) \mathbf{e}_{\theta_v} \cdot \mathbf{e}_{y_{c2}} = \frac{V_\theta^{\max} r_0}{(1 - e^{-a^2})} \frac{(1 - e^{-\alpha(r^2/r_0^2)})}{r^2} [-C_{span} z_{c2} + C_{chord}(x_{c2} - U_c t)]. \quad (9)$$

with $C_{span} = (\cos\beta + \tan\beta)\cos(\varphi + \gamma_2)$ and $C_{chord} = \sin^2(\varphi + \gamma_2)\sin(\beta)$. The subscripts *span* and *chord* were chosen because the projections are related either to the chord (x_{c2}) or span (z_{c2}) variables. r is the radius expressed in the aft blade reference frame (x_{c2}, y_{c2}, z_{c2}) :

$$r(x_{c2}, 0, z_{c2}, t) = \sqrt{(c_\beta z_{c2})^2 + \sin(\gamma_2 + \varphi)^2 (x_{c2} - U_c t)^2}, \quad (10)$$

where $c_\beta = \sqrt{1 + \tan^2(\beta)}$ is the new coefficient expanding the radius because of the 3D path and $U_c = \Omega R_{VI} \sin(\gamma_2) / \sin(\gamma_2 + \varphi)$ is the phase velocity of the vortex. The rotational speed $\Omega_2 - \Omega_1 = \Omega$ is chosen because the vortices are represented in the front-rotor reference frame. Though U_c does not coincide with the relative flow speed (obtained by speed triangles), both are assumed equal for the purpose of this paper. This assumption is made because both velocities are close in the current configuration. However if it is not the case, a free-stream to convection speed ratio correction presented by Roger and Moreau [37] needs to be applied. The upwashes for the other vortex models are written as

$$\begin{aligned} w^{Sc}(x_{c2}, 0, z_{c2}, t) &= \frac{V_\theta^{\max} \sqrt{2}}{r_0} \frac{1}{((r/r_0)^2 + 1)} [-C_{span} z_{c2} + C_{chord}(x_{c2} - U_c t)], \\ w^{Ta}(x_{c2}, 0, z_{c2}, t) &= \frac{V_\theta^{\max}}{r_0} e^{1-r/r_0} [-C_{span} z_{c2} + C_{chord}(x_{c2} - U_c t)]. \end{aligned} \quad (11)$$

For a pure 2D case ($\beta = 0$), the above formulas exactly yield the 2D upwashes formulas derived by Roger et al. [9]. As mentioned in Section 2 the OBVI mechanism for CROR is a periodic mechanism related to the blade-passing period

corresponding to the counter-rotating motion of the rotors. The upwashes are thus derived in the frequency domain. This procedure is similar to what is performed for the wake interaction noise in turbomachinery [38]. The convention for the Fourier transform is $\exp(-i\omega t)$ for monochromatic waves and positive frequencies. For the sake of conciseness only the Lamb-Oseen result will be displayed at this stage. It reads [39]:

$$\begin{aligned}\tilde{w}^{LO}(x_{c2}, 0, z_{c2}, \omega) &= \frac{1}{2\pi} \int_{-\infty}^{+\infty} w^{LO}(x_{c2}, 0, z_{c2}, t) e^{i\omega t} dt \\ &= \frac{-V_{\theta}^{max} r_0}{1 - e^{-\alpha^2}} \frac{e^{-ik_x x_{c2}}}{4U_c \sin(\varphi + \gamma_2)} \left[C_{span} \frac{h(-z_{c2}) - h(z_{c2})}{c_{\beta}} + i C_{chord} \frac{h(-z_{c2}) + h(z_{c2})}{\sin(\varphi + \gamma_2)} \right],\end{aligned}\quad (12)$$

with

$$h(z_{c2}) = e^{ik_x z_{c2} / \sin(\varphi + \gamma_2)} \left[1 - \operatorname{erf} \left(\frac{k_x r_0}{2 \sin(\varphi + \gamma_2)} + \frac{z_{c2}}{r_0} \right) \right]. \quad (13)$$

$k_x = \omega/U_c$ is the chordwise wavenumber of the incoming gusts and erf is the error function [40]. Up to now, only the upwash produced by a single vortex is modeled. Yet, the adjacent front-rotor blade sheds a similar vortex that impinges the same aft blade at $t_{adj} = t + \Delta t$. $\Delta t = 2\pi/(B_1\Omega)$ is the delay between two consecutive BVI events. B_1 is the front rotor blade number. For the CROR case, the resulting vortex train reads using a convolution product:

$$f_w(t) = \sum_{n=-\infty}^{+\infty} w(x_{c2}, 0, z_{c2}, t - n\Delta t) = w(x_{c2}, 0, z_{c2}, t) \star \sum_{n=-\infty}^{+\infty} \delta(t - n\Delta t). \quad (14)$$

The Fourier series of the above train of vortices gives:

$$\tilde{f}_w(\omega) = \sum_{n=-\infty}^{+\infty} \frac{2\pi n}{\Delta t} \tilde{w}(x_{c2}, 0, z_{c2}, \omega) \delta(\omega - n2\pi/\Delta t). \quad (15)$$

It means that the periodic vortex train selects discrete frequencies. The interaction can therefore be assessed at a single frequency from any expression of \tilde{w} . The final step for the upwash derivation part is now to turn the upwashes into a distribution of sinusoidal gusts in the chordwise (following x_{c2}) and spanwise (z_{c2}) directions. Sinusoidal gusts are required by Schwarzschild's technique in order to compute the unsteady pressure jump on the blade. This yields:

$$\tilde{G}(k_x, k_z) = \frac{1}{2\pi} \int_{-\infty}^{+\infty} [\tilde{w}(x_{c2}, 0, z_{c2}, \omega) e^{-ik_x x_{c2}}] e^{-ik_z z_{c2}} dz_{c2}. \quad (16)$$

The spatial gust spectra $\tilde{G}(k_x, k_z)$ are derived for each aforementioned vortices:

$$\begin{aligned}\tilde{G}^{LO}(k_x, k_z) &= \frac{i C_{amp}^{LO}}{2\pi U_c \sin(\varphi + \gamma_2)} \left[\frac{C_{span} k_z}{c_{\beta}} - \frac{C_{chord} 2abk_x}{\sin(\varphi + \gamma_2)} \right] \frac{e^{-a^2 k_x^2 - \frac{k_z^2}{4b^2}}}{(2abk_x)^2 + k_z^2}, \\ \tilde{G}^{Sc}(k_x, k_z) &= -\frac{C_{amp}^{Sc} r_0^2}{4\pi U_c \sin(\varphi + \gamma_2)} \left[-k_z C_{span} + \frac{k_x C_{chord}}{c_{\beta} \sin^2(\varphi + \gamma_2)} \right] \frac{2i r_0}{\sqrt{k_x^2 + c_{\beta}^2 k_x^2 / \sin^2(\varphi + \gamma_2)}} K_1 \left(\frac{r_0}{c_{\beta}} \sqrt{k_x^2 + \frac{c_{\beta}^2 k_x^2}{\sin^2(\varphi + \gamma_2)}} \right), \\ \tilde{G}^{Ta}(k_x, k_z) &= \frac{C_{amp}^{Ta} \sqrt{2\pi} i r_0^2}{c_{\beta}} \left[\frac{r_0 k_z C_{span}}{c_{\beta}^2 \sqrt{2\pi}} - \frac{r_0 k_x C_{chord}}{\sin^2(\varphi + \gamma_2)} \right] e^{-\frac{r_0^2 k_x^2}{2c_{\beta}^2}},\end{aligned}\quad (17)$$

where C_{amp}^{LO} , C_{amp}^{Sc} and C_{amp}^{Ta} are respectively equal to $V_{\theta}^{max} r_0 / (1 - \exp(-\alpha^2))$, $V_{\theta}^{max} \sqrt{2} / r_0$ and $V_{\theta}^{max} \sqrt{e} / r_0$. $a = r_0 / (2\sqrt{\alpha} \sin(\varphi + \gamma_2))$ and $b = \alpha c_{\beta} / r_0$ are related to the chordwise and spanwise developments of the Lamb-Oseen vortex. K_1 is the modified Bessel function [41]. Eq. (17) for the 3D upwash wavenumber spectra have been verified in 2 ways. On the one hand, a 3D pattern is valid if its value yields the 2D case derived by Roger et al. [9] when $\beta = 0^\circ$ (Fig. 10(a)).

On the other hand, the validation assesses the direction and the amplitude of the rotation (Fig. 10(b)). All models need to rotate in the same direction counterclockwise for positive stream-tube contraction angle with the same angle (Fig. 11). The rotational angle of the upwash distribution, because of the projections with different axes, is not equal to β . The resulting spectral distributions for the two vortices with circulation (Lamb-Oseen and Scully) are alike (Figs. 11(a) and (b)). They have two symmetric lobes with a symmetry line related to the stream-tube contraction effect. However, the vortex without total circulation (Fig. 11(c)) exhibits a different spectral distribution. The maximum is now located at $k_z^{max} = 1/r_0$, meaning that the energy of the vortex is concentrated within the core. The magnitude of the spectral energy for the vortex without circulation is lower than that of the vortices with circulation. It means that vortices without circulation are likely to produce a less intense OBVI noise.

The same work has been performed on the axial velocity deficit, it yields:

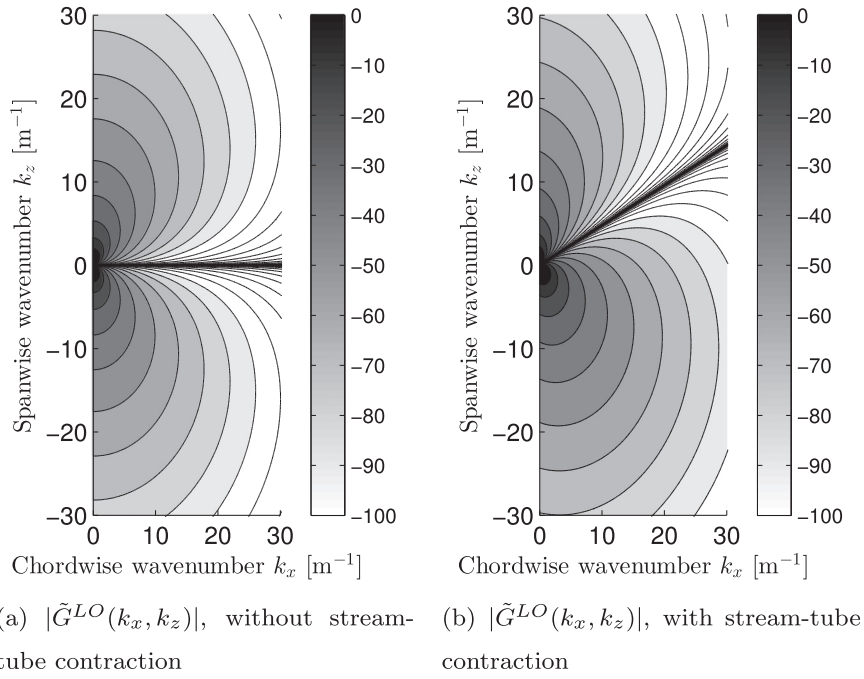


Fig. 10. Upwash wavenumber spectra \tilde{G} , with and without stream-tube contraction angle (β), $V_\theta^{max} = 30 \text{ m} \cdot \text{s}^{-1}$, $r_0 = 0.07 \text{ m}$, $\varphi = 28^\circ$, $\beta = 11^\circ$. Values are shown in logarithmic scale: $20\log_{10}(|\tilde{G}|)$.

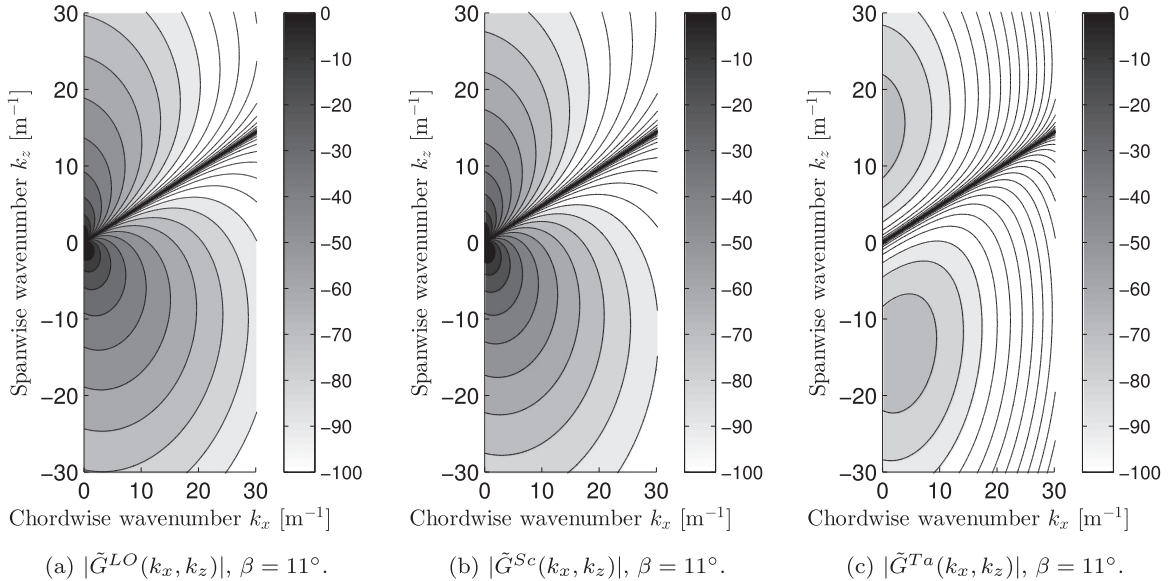


Fig. 11. Upwash wavenumber spectra \tilde{G} for different vortex models, logarithmic scale: $20\log_{10}(|\tilde{G}|)$.

$$\tilde{G}^{zv}(k_x, k_z) = \frac{-V_x^{max} \cos(\beta) r_0}{4\pi U_c c_\beta} \exp \left[- \left(\frac{k_x r_0}{2 \sin(\varphi + \gamma_2)} \right)^2 - \left(\frac{k_z r_0}{2 c_\beta} \right)^2 \right]. \quad (18)$$

As expected the upwash spectrum for the axial velocity deficit has also a 2D Gaussian shape [42]. The influence of the stream-tube contraction is minimal (Fig. 12); it only increases the radius of the vortex projected on the blade (r_0/c_β).

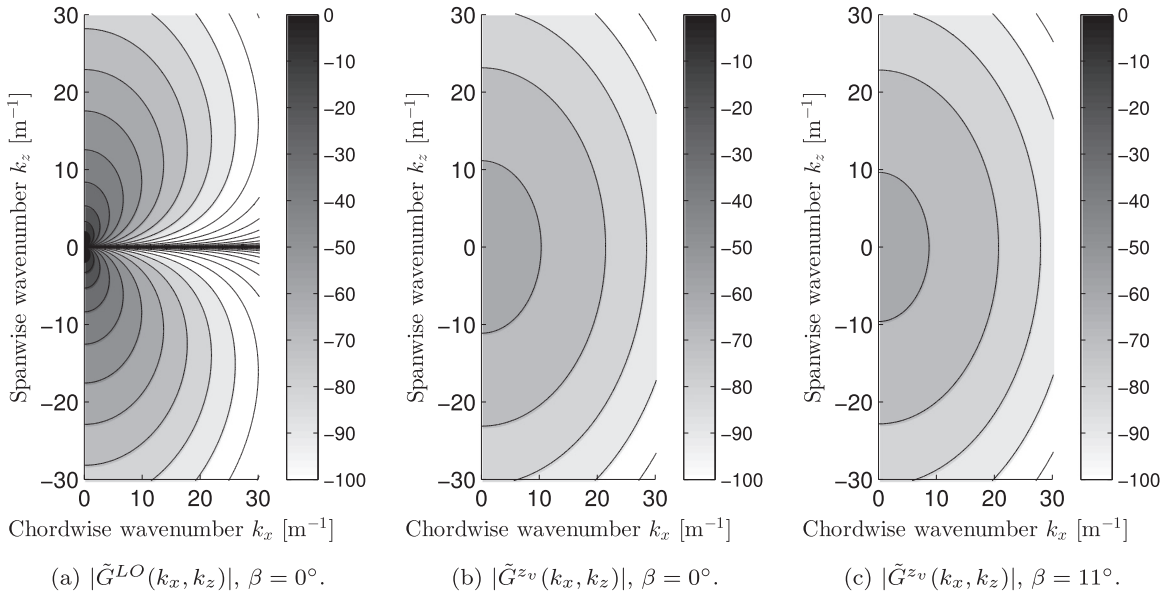


Fig. 12. Upwash wavenumber spectra \tilde{G} , $v_x^{max} = 12 \text{ m} \cdot \text{s}^{-1}$, other parameters set as in Fig. 10. Logarithmic scale: $20\log_{10}(|\tilde{G}|)$.

5. Unsteady pressure jump results

Having described the upwash excitation, the blade response can then be computed for each incoming gust. The unsteady aerodynamics is derived from Amiet's theory [21], adapted for the case of infinitely thin, swept, finite chord (c), infinite span airfoils using the linearized theory [22,9,43]. Fig. 13 shows the flat plate representing the aft-blade. Only the stagger and sweep angles are used in order to represent the interaction. The lean angle is discarded in the current study, which is an additional geometrical simplification compared with the actual geometry. However, at the OBVI locus, the flat plate represents the real blade fairly well.

A sinusoidal upwash described by $w(x'_{c2}, z'_{c2}, t) = \tilde{G}(k_x, k_z)\exp(i(k'_x x'_{c2} + k'_z z'_{c2} - \omega t))$ is convected over the airfoil at the oblique speed $\mathbf{U}_0 = U_1 \mathbf{e}_{x'_{c2}} + U_2 \mathbf{e}_{z'_{c2}}$ with $|\mathbf{U}_0| = U_c$. The reference frame $(x'_{c2}, y_{c2}, z'_{c2})$ is related to the swept blade reference frame presented in Section 2 in Fig. 2(d). The sweep redefines the wavenumbers of the upwash spectral content $\tilde{G}(k_x, k_z)$ according to Ψ . The upwash spectral content is selected from the rotated wavenumbers k'_x and k'_z defined by:

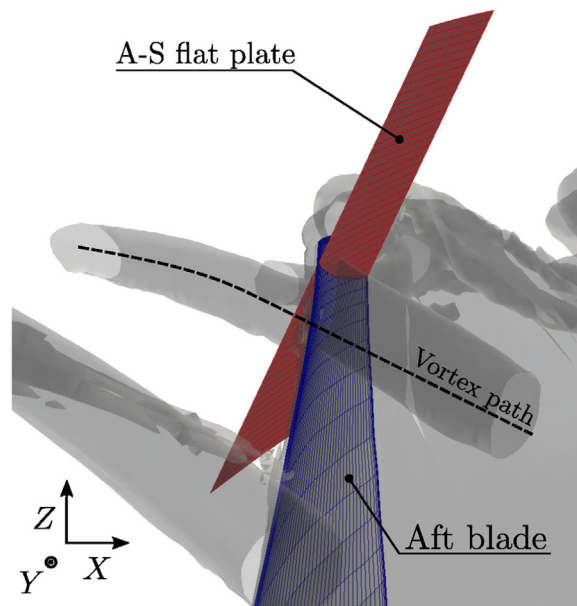


Fig. 13. Aft-blade geometry for loading computation in the global reference frame. Grey surfaces are iso-surfaces of entropy extracted from CFD.

$$k_x = \cos \Psi k'_x + \sin \Psi k'_z, \quad k_z = -\sin \Psi k'_x + \cos \Psi k'_z. \tag{19}$$

The impingement of the gust generates a potential velocity disturbance $\vec{u}' = \nabla \Phi'$ (considering an irrotational velocity disturbance) such that Φ' is the solution of the general convected Helmholtz equation:

$$\beta_1^2 \frac{\partial^2 \Phi'}{\partial^2 x'_{c2}} + \beta_2^2 \frac{\partial^2 \Phi'}{\partial^2 z'_{c2}} + \frac{\partial^2 \Phi'}{\partial^2 y'_{c2}} + 2i k \left(M_1 \frac{\partial \Phi'}{\partial x'_{c2}} + M_2 \frac{\partial \Phi'}{\partial z'_{c2}} \right) - 2M_1 M_2 \frac{\partial^2 \Phi'}{\partial x'_{c2} \partial z'_{c2}} + k^2 \Phi' = 0, \tag{20}$$

where $k = \omega/c_0$ is the gust wavenumber, $\beta_1 = \sqrt{1 - M_1^2}$ and $\beta_2 = \sqrt{1 - M_2^2}$ are the chordwise and spanwise compressibility coefficients respectively, M_1 and M_2 being the corresponding Mach numbers. The boundary conditions of the problem are:

- Zero potential upstream of the leading-edge: $\Phi' = 0, x'_{c2} < 0$.
- Zero normal velocity on the airfoil surface: $\frac{\partial \Phi'}{\partial y'_{c2}}(x'_{c2}, 0, z'_{c2}) = 0, 0 < x'_{c2} < c$.
- Zero pressure jump at the trailing-edge and in the wake (Kutta condition): $\bar{p}'(x'_{c2}, 0, z'_{c2}) = 0, x'_{c2} > c$,

using the material derivative D/Dt in order to link the pressure and the velocity potential together:

$$\bar{p}'(x'_{c2}, 0, z'_{c2}) = -\rho_0 \frac{D(\Phi')}{Dt} = -i \omega \Phi' + U_1 \frac{\partial \Phi'}{\partial x'_{c2}} + U_2 \frac{\partial \Phi'}{\partial z'_{c2}}. \tag{21}$$

A canonical Helmholtz equation is obtained assuming that Φ' is an infinite combination of sinusoidal gusts with different obliqueness (different k_z values) and assuming a transformed velocity potential $\Phi' = \Phi' \exp(iM_1^2 k'_x x'_{c2} / \beta_1^2)$. With dimensionless coordinates (x'^*_2, y'^*_2, z'^*_2) and wavenumbers $(k'_x, 0, k'_z)$ using the lengthscales $(1, \beta_1, \beta_1)2/c$, Eq. (21) reads:

$$\frac{\partial^2 \Phi'}{\partial^2 x'^*_2} + \frac{\partial^2 \Phi'}{\partial^2 y'^*_2} + \kappa^2 \Phi' = 0, \tag{22}$$

where

$$\kappa^2 = \mu^2 \left(1 - \frac{1}{\theta^2} \right), \quad \mu = \frac{k'_x M_1}{\beta_1} \quad \text{and} \quad \theta = \frac{\mu \beta_1}{k'_z}. \tag{23}$$

The sign of κ^2 is related to the phase velocity of the incoming gusts and changes the nature of the partial differential Eq. (21) [43]. Supersonic gusts ($\kappa^2 > 0$, i.e hyperbolic equation) give strong propagating pressure waves along the chord (solid lines in Fig. 14) whereas subsonic gusts ($\kappa^2 < 0$, i.e elliptic equation) give evanescent pressure waves which quickly go to zero away from the leading-edge (dashed lines in Fig. 14). Despite their lower influence compared with supercritical gusts (solid lines in Fig. 14), subcritical gusts contribute to the radiation integral in the far-field because of the finite span [41,37,23]. For clarity sake, the inverse square-root singularity is removed from the induced-pressure plots by multiplying by $\sqrt{x'^*_2}$ in Fig. 14.

Both the stream-tube contraction angle (β) and the sweep angle (Ψ) have a direct influence on the κ parameter. As

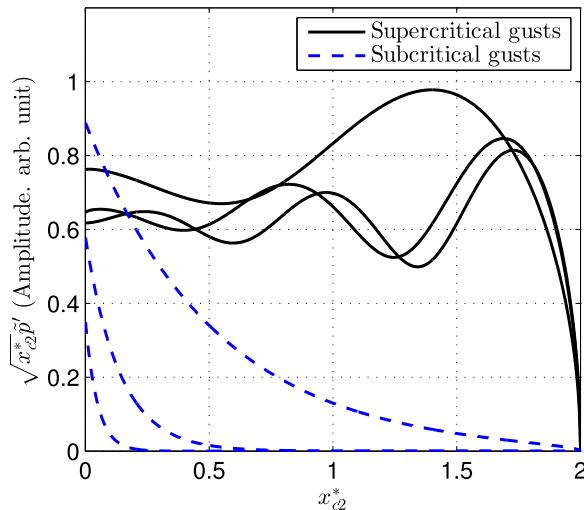


Fig. 14. Typical regularized pressure distributions ($\sqrt{x'^*_2} \bar{p}'$) for different skewed gusts. Solid lines: supercritical gusts. Dashed lines: subcritical gusts.

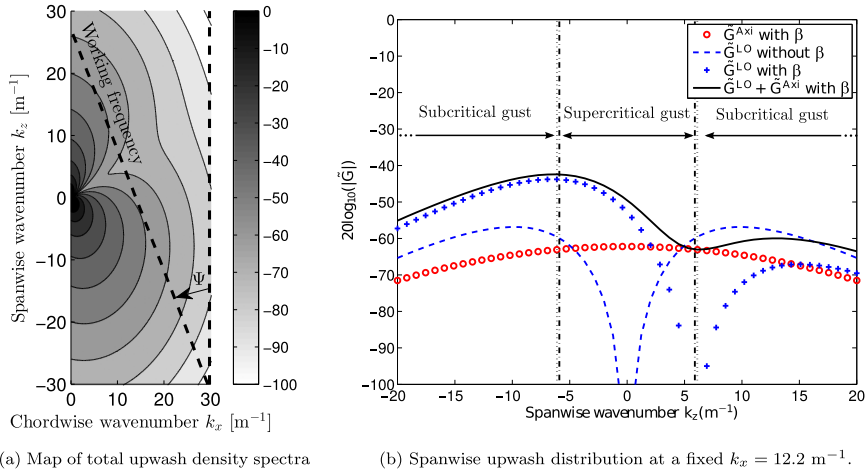


Fig. 15. Distribution of skewed gust spectra for the first loading harmonic $k_x = B_1|\Omega_1 - \Omega_2|/U_c$. The vertical lines show the transition from the supercritical to the subcritical region. Dotted lines are the transition with the stream-tube contraction, point-dotted lines are the transition without the stream-tube contraction.

previously seen in Section 4, the stream-tube contraction angle rotates the upwash spectrum around the (0,0) point. For the tangential velocity, it means that more energy will be located in the supercritical area (Fig. 15). It also indicates that the incoming velocity is skewed in the (x_{c2}^*, z_{c2}^*) reference frame. This 2D convection velocity is similar to a swept-blade effect. Slight sweep reduces the supercritical area (Fig. 15(b)) because U_1 is used as chordwise velocity instead of $|U_0|$. The effect of sweep is particularly important when gusts switch from supercritical to subcritical [44]. In Fig. 2(d), the stream-tube contraction angle is shown to have an opposite effect to the sweep as the chordwise velocity is increased. In Fig. 15(b) this effect explains a slightly larger supercritical range for the full model (stream-tube contraction and sweep). As expected, the loading is symmetric for the zero-sweep, zero stream-tube contraction case and asymmetric otherwise.

Through an iterative use of Schwarzschild's procedure [45], a closed-form solution of Eq. (22) with the aforementioned boundary conditions can be found. Schwarzschild's solution is given for the scattering of a sinusoidal wave by the edge of an infinite half-plane. First the leading-edge gust impact problem is solved for a semi-infinite chord profile, then the trailing-edge pressure back-scattering problem is solved in order to correct the first solution according to the Kutta condition. The main leading-edge and trailing-edge correction pressure-jumps are:

$$\begin{aligned} \tilde{I}_{LE}(x_{c2}^*, 0, z_{c2}^*) &= -\rho_0 U_1 \tilde{G}(k_x, k_z) \frac{\exp(-i(\mu M_1 - \kappa)x_{c2}^* + i k_z^* z_{c2}^* + i \pi/4) \exp(-i \omega t)}{\sqrt{\pi(k_x^* + \beta_1^2 \kappa)x_{c2}^*}}, \\ \tilde{I}_{TE}(x_{c2}^*, 0, z_{c2}^*) &= \rho_0 U_1 \tilde{G}(k_x, k_z) \\ &\times \frac{\exp(-i(\mu M_1 - \kappa)x_{c2}^* + i k_z^* z_{c2}^* + i \pi/4) \exp(-i \omega t)}{\sqrt{\pi(k_x^* + \beta_1^2 \kappa)}} [1 - (1 + i)E^*(2\kappa(x_{c2}^* - 2))]. \end{aligned} \tag{24}$$

E^* is the complex conjugate of the Fresnel integral as defined by Amiet [21]:

$$E^*(x) = \int_0^x \frac{e^{-i\xi}}{\sqrt{2\pi\xi}} d\xi. \tag{25}$$

These unsteady pressure-jump formulas are twice the disturbance pressure since pressure fluctuations (\tilde{p}') have opposite phases on both sides. The aforementioned formulas are valid for supercritical gusts. For subcritical gusts, a modified value of $i\kappa' = i\sqrt{-\kappa^2}$ is used, the Fresnel integral E^* becomes $1 - \text{erf}(\sqrt{2\kappa'(2 - x_{c2}^*)})$. In principle, Schwarzschild's technique breaks down as the parameter κ goes to zero, at the transition between the supercritical and sub-critical regimes. This is the possible origin of discontinuities in computations that involve both kinds of gusts, as already pointed out in the complementary problem of airfoil trailing-edge noise [37]. The issue was solved by performing an interpolation to smooth the discontinuities out. Adamczyk also noted that around the transition classical Sears' solution corrected for compressibility effects could be used as an alternative [46]. But in the present case no evidence of discontinuity has been found, which suggests that, though possible in principle, it is not a practical issue. Moreover, as also pointed out by Adamczyk, the iterative process is valid for large values of $|\kappa|$. Yet differences with the exact solution remain limited as shown by Adamczyk [46] and more recently by Moreau and Roger [47]. For this reason, the present results only include the implementation of Amiet-Schwarzschild's approach.

Fig. 16 shows the total pressure jump ($\tilde{I}_{tot} = \tilde{I}_{LE} + \tilde{I}_{TE}$) produced by a OBVI event using different vortex models on a swept blade. Both supercritical and subcritical gusts are taken into account. A BVI event using the Lamb-Oseen (Fig. 16(a)) and Scully vortices (Fig. 16(b)) give similar responses. The pattern is similar to two independent dipoles with opposite phases

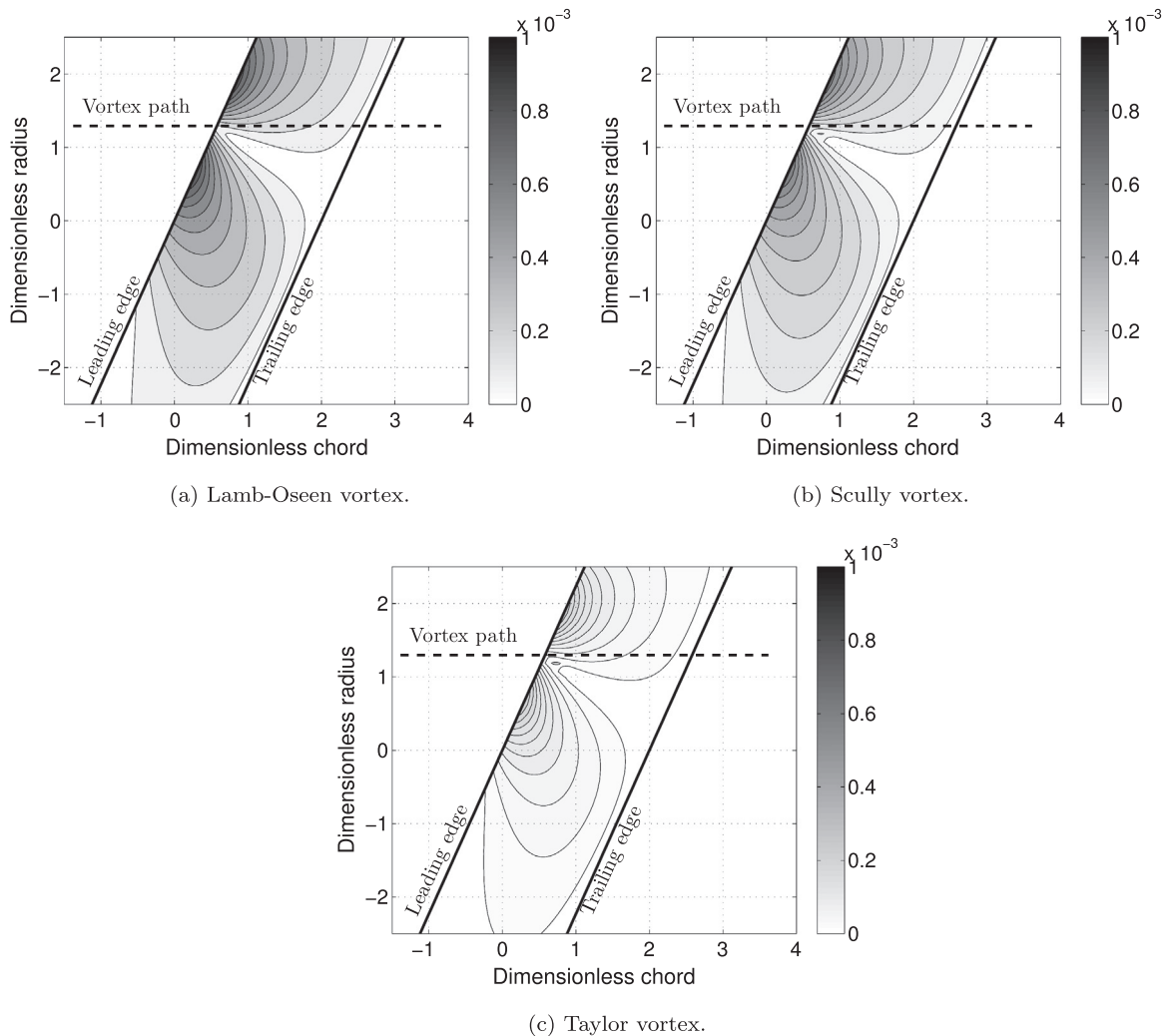


Fig. 16. $|\sqrt{x_{c2}^*} \tilde{I}_{tot}|$ values on the blade for the first loading harmonic. The vortex centerline is represented in dashed line impacting from left to right. x_{c2}^* and z_{c2}^* are the dimensionless chordwise and spanwise directions respectively, $\Psi = 28^\circ$, $\beta = 0^\circ$, same parameters as in Fig. 10. Pressure are made dimensionless using the atmospheric pressure $p_{atm} = 101325$ pa.

pulsating close together which is likely to produce some noise cancellation in the far field. As mentioned in the upwash spectrum analysis section, the blade response produced by an OBVI is less intense for a vortex without circulation. These results are consistent with numerical investigations performed by Falissard and Delattre [15]. Numerical results also showed that for vortices with circulation, the two dipoles with opposite phases are asymmetric. This additional effect may come from the gradient of convection velocity along the span which is not presently modeled.

Using the Lamb-Oseen vortex only, the influence of the stream-tube contraction is shown in Fig. 17. Seemingly, the stream-tube contraction angle largely unbalances the two lobes with opposite phases seen in Fig. 16. This effect is likely to turn off the noise cancellation effect produced by the equal dipoles with opposite phases. This lopsided effect produced by the stream-tube contraction is caused by the local projection of the vortex radius on the blade. The interaction has an upwash part and a downwash part which are symmetric if the vortex trajectory is not influenced by the stream-tube contraction. Adding the stream-tube contraction makes one side impact the blade with more intensity whereas the other side is grazing the surface. Asymptotically, a 90° stream-tube contraction angle turns the orthogonal BVI interaction into a parallel BVI [48]. As already seen in Fig. 11, the unbalance process is explained by the spectrum energy rotation which shifts energetic gusts inside the supercritical area.

Finally, the influence of the axial velocity deficit is tested in Fig. 18. Fig. 18(b) exhibits a single, concentrated, intense lobe. The axial velocity deficit has a single upwash or downwash lobe which is linked to the sign of V_x^{max} . The present results use the same maximum velocity ratio (V_θ^{max}/V_x^{max}) extracted from CFD. Because the axial and tangential velocities are orthogonal and because the aforementioned model is linear, the contribution of both velocities can be summed to yield a total upwash spectrum:

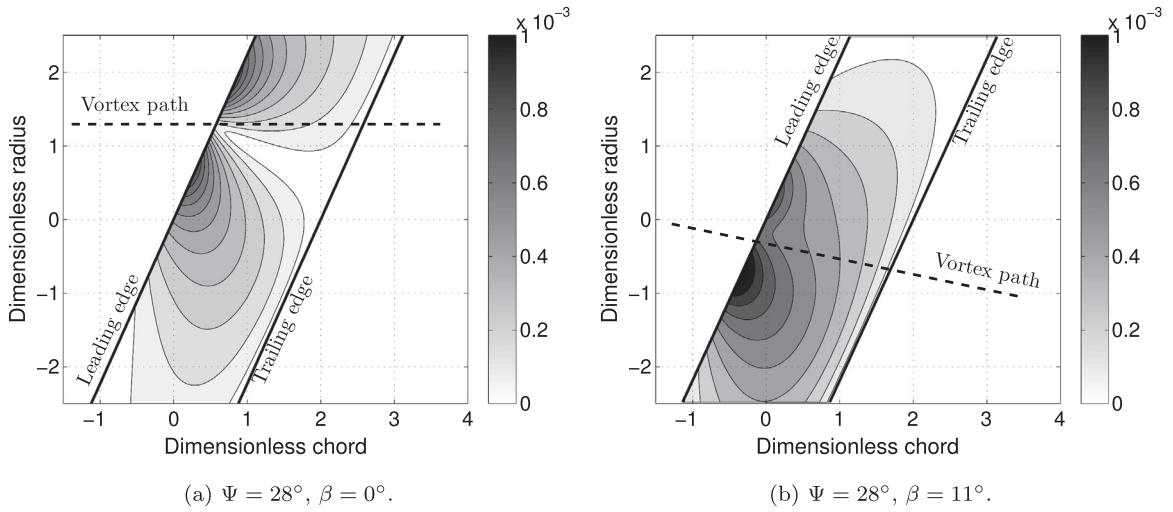


Fig. 17. $|\sqrt{x_{c2}^* \tilde{t}_{tot}}|$ values on the blade. The vortex centerline is represented in dashed line impacting from left to right. x_{c2}^* and z_{c2}^* are the dimensionless chordwise and spanwise directions respectively, same parameters as in Fig. 10.

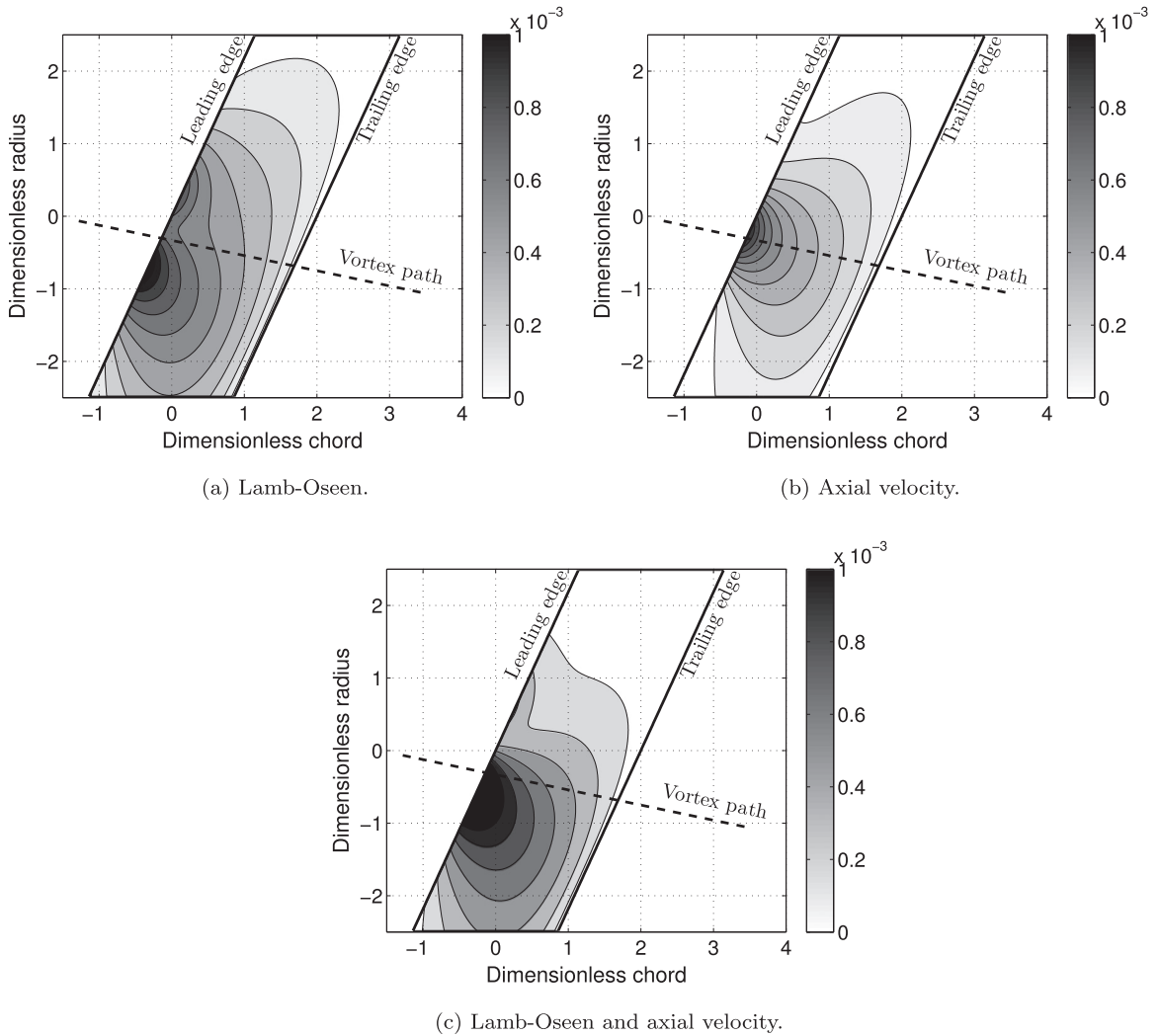


Fig. 18. $|\sqrt{x_{c2}^* \tilde{t}_{tot}}|$. Influence of the axial velocity deficit, $\Psi = 28^\circ, \beta = 11^\circ, V_x^{max} = 0.4V_\theta^{max}$, same parameters as in Fig. 10.

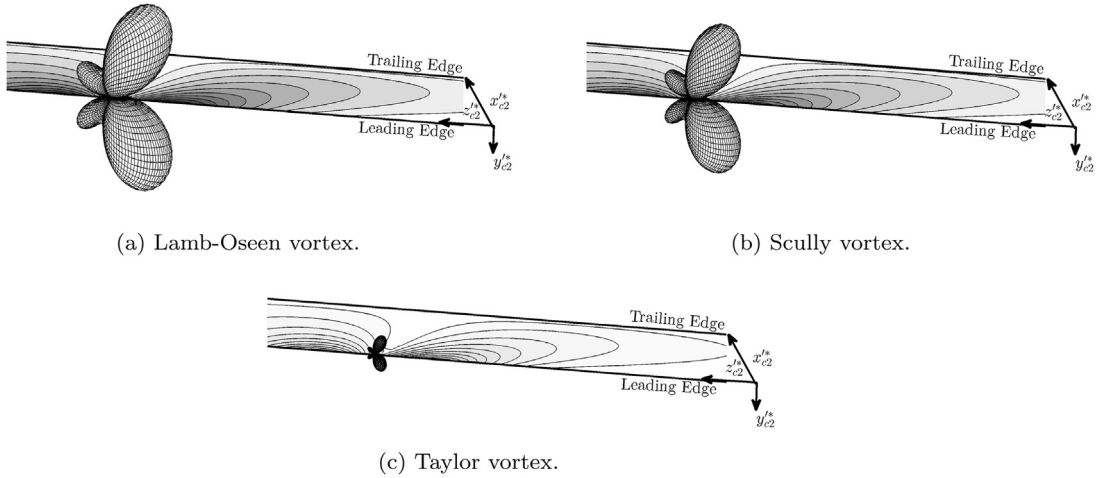


Fig. 19. Acoustic lobes for different vortices, $|\bar{p}(x_{c2}, y_{c2}, z_{c2}, \omega)|$, $\Psi = 0^\circ$, $\beta = 0^\circ$, same scale, observer at $\sqrt{x_{c2}^2 + y_{c2}^2 + z_{c2}^2} = R = 1$ m, same BVI parameters as in Fig. 10.

$$\tilde{G}^{tot} = \tilde{G}^{zv} + \tilde{G}^* \tag{26}$$

with the superscript \star referring to one of the upwash spectrum formula derived from the tangential velocity models (Eqs. (4)). For the full 3D vortex (Fig. 18(c)), the result on the pressure is similar to the stream-tube contraction. One lobe is enhanced by the axial velocity deficit whereas the other lobe is reduced. Because the influence of the axial velocity is more localized than the tangential velocity, the reduced lobe is unaffected by the axial velocity away from the vortex core in Fig. 18(c). This lobe imbalance will again modify the dipoles with opposite phases, which is going to impact the acoustics of the OBVI event thereafter presented.

6. Acoustic results

Having the blade response to the upwash gust, the far-field acoustic pressure can be obtained with Curle's analogy for a fixed surface [49]. The radiation problem is considered in the RF of the blade. This corresponds to what would be received by an observer moving with the blade and gives an indication on the natural directivity of the sources. It is assumed that only the loading noise produced by the unsteady pressure acting on a blade embedded in a uniform flow is significant. Amiet's blade responses are considered as equivalent distributed dipoles along the chord length. Therefore, the far-field acoustic pressure for an observer located at (x_{c2}, y_{c2}, z_{c2}) is given by:

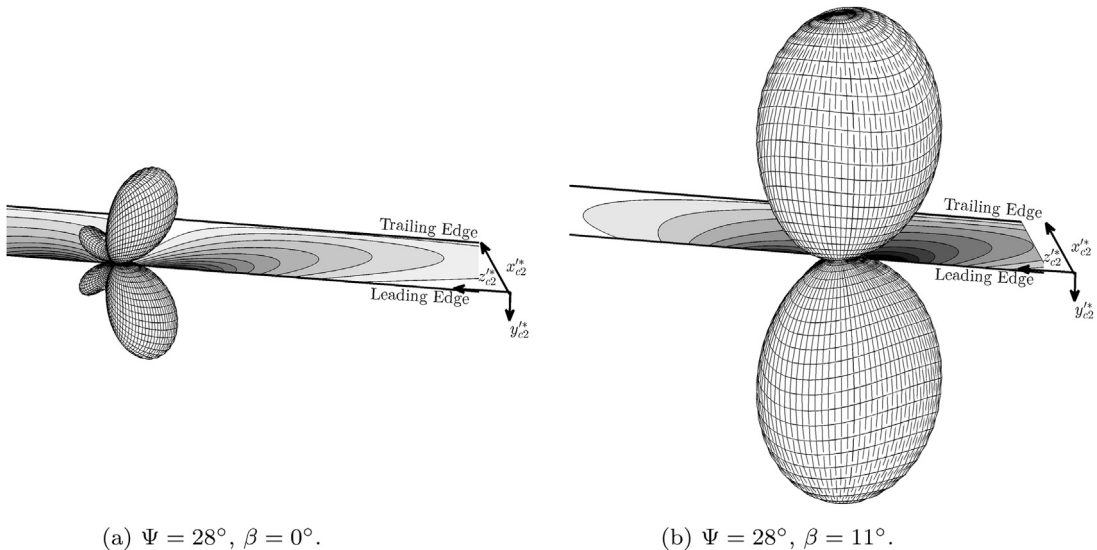


Fig. 20. Acoustic directivity lobes $|\bar{p}(x_{c2}, y_{c2}, z_{c2}, \omega)|$ for the Lamb-Oseen vortex, same scale, observer at $R = 1$ m, same BVI parameters as in Fig. 10.

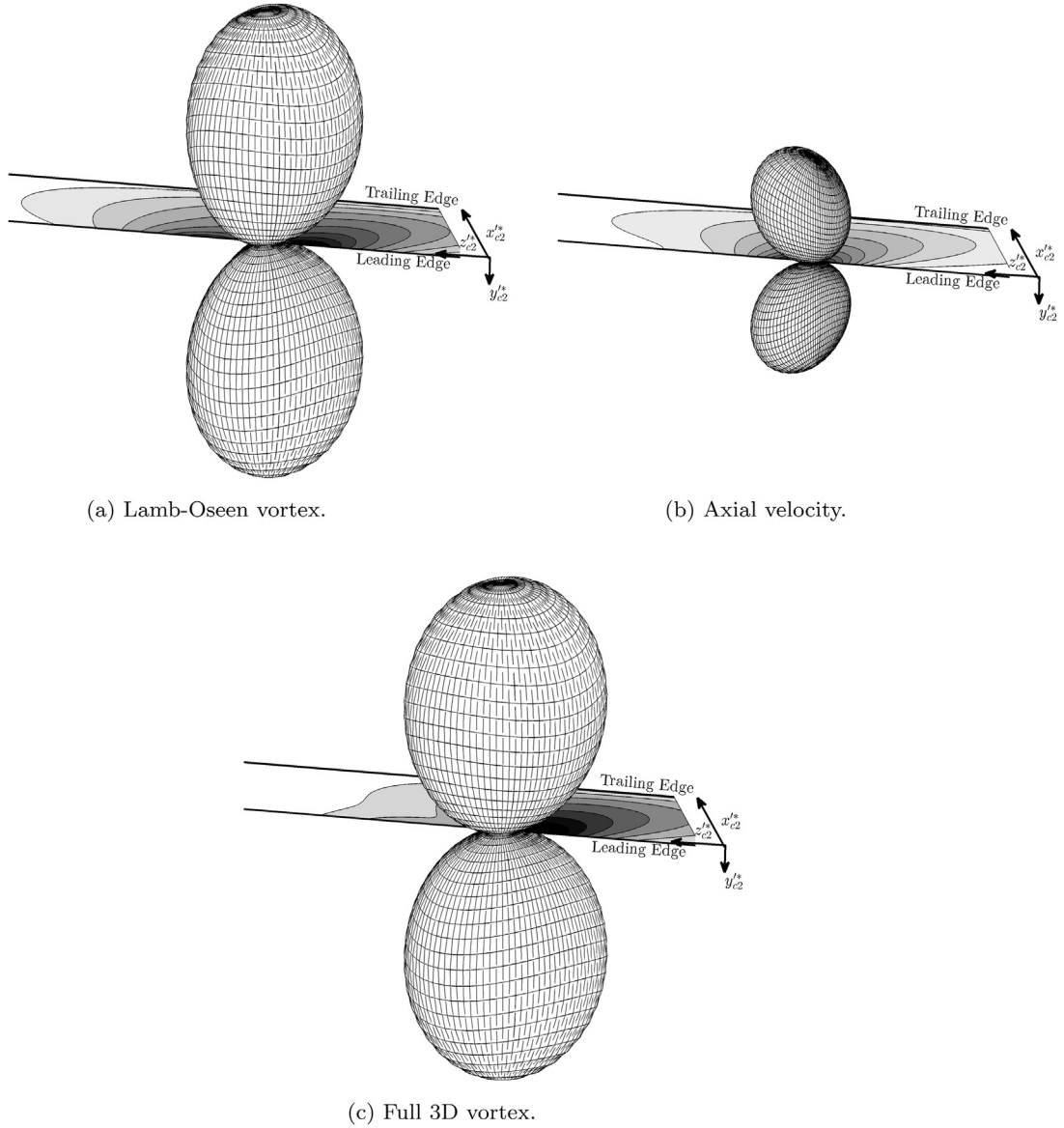


Fig. 21. Acoustic directivity lobes for different vortices, $|\bar{p}(x_{c2}, y_{c2}, z_{c2}, \omega)|$, $\Psi = 28^\circ$, $\beta = 11^\circ$, same scale, observer at $R = 1$ m, same BVI parameters as in Fig. 10.

$$\bar{p}(x_{c2}, y_{c2}, z_{c2}, \omega) = \frac{i k^* y_{c2} C}{8\pi S_0^2} \cos \Psi \int_{-\infty}^{+\infty} \int_0^{2/\cos \Psi} \bar{I}_{tot}(x_{c2}^*, z_{c2}^*) e^{i k^* (M_2 - \beta_1^2 z_{c2}/S_0) z_{c2}^*/\beta^2} e^{i k^* (M_1 - \beta_2^2 x_{c2}/S_0) \cos \Psi} e^{i k^* (M_2 - \beta_1^2 z_{c2}/S_0) \sin \Psi x_{c2}^*/\beta^2} dx_{c2}^* dz_{c2}^*, \quad (27)$$

where $S_0 = [x_{c2}^2 + \beta^2(y_{c2}^2 + z_{c2}^2)]^{1/2}$ is the convection-corrected distance. The origin of the reference frame is defined at the leading-edge tip location (0,0). For a rectangular geometry, a closed-form solution can be derived from Eq. (27). The directivity diagrams of the Lamb-Oseen, Scully and shielded Taylor vortices are presented in Fig. 19. For a better understanding they are plotted as 3D surfaces of arbitrary amplitude (the same for all plots) superimposed on a view of the flat plate, with the origin at the vortex impingement point. The two dipoles with opposite phases indeed create an acoustic lateral quadrupole. As expected, the OBVI using a vortex without circulation gives a lower acoustic pressure than the models with circulation but the global directivities are identical and compare fairly well with the numerical results of Falissard and Delattre [15] obtained with a high-order Euler code on a constant-chord twisted blade made of thin NACA-0002 airfoils (Figs. 15–17 in [15]).

Fig. 20 shows that both the stream-tube contraction and the sweep break the symmetry of the two dipoles with opposite phases. For the swept case (Fig. 20(b)), it slightly reduces the overall acoustic energy produced by the OBVI event because of the reduced supercritical range. On the contrary, the stream-tube contraction quickly unbalances the dipoles and turns the radiation into a highly efficient dipolar source despite a reduced supercritical range. Moreover, the preferred directivity of the sound is not purely perpendicular to the blade but skewed depending on the value of the β angle. This imbalance is strong for low values of the stream-tube contraction angle, making the stream-tube contraction angle a significant parameter to investigate for CROR BVI tonal noise.

Fig. 21 shows that the acoustic pressure of the pure axial velocity deficit is clearly dipolar. Even if the maximum velocity of the axial velocity is half the maximum of the tangential velocity, the resulting acoustic pressure is higher for a pure axial velocity BVI event. The combination of the two velocity components gives a slightly asymmetric dipolar radiation. For an unswept, zero stream-tube contraction case and using the geometrical parameters presented in Fig. 10, the axial velocity is dominating the interaction. This result agrees with another similar BVI case seen in helicopters when tip vortices from the main rotor impinge on the rear rotor [48,50]. However, for the CROR case, the tangential velocity has still an important role, particularly when comparing results from Figs. 20(b) and 21(c). A moderate stream-tube contraction gives higher dipolar radiation than the axial velocity deficit so that both velocities still need to be taken into account.

7. Conclusions

An analytical model for CROR-OBVI tonal noise, initially developed for a 2D Lamb-Oseen vortex impinging on the blade at constant radius, has been extended to more general 3D vortex models accounting for the important axial velocity, impinging on the rear blade at an angle representing the stream-tube contraction observed for particular CROR regimes such as approach or take-off. The effect of the vortex circulation and its link with the outside-core decay rate is also investigated. It confirms the results already obtained with numerical simulations [15] or experiments [33]. The Lamb-Oseen vortex like other vortices with circulation also compares more favorably to a detailed URANS simulation. The diffusion of the vortex along its trajectory can also be accounted for. Only its distortion is omitted in the present model.

The stream-tube contraction tends to unbalance the pressure patterns with opposite phases induced on the blade by the upwash and downwash parts of the impingement. Unlike what was found previously without contraction, this gives asymmetric acoustic lobes. Even for low stream-tube contraction angles, the asymmetry turns the lateral quadrupole obtained by symmetric pressure lobes with opposite phases into a strong skewed dipole. The strength of this dipole comes from the rotation of the highly energetic gusts inside the supercritical area of the two-dimensional wavenumber spectrum.

The axial velocity deficit plays a role on both the directivity and the level of the radiated sound. For these particular geometrical conditions, the axial velocity deficit is the dominant noise source of the OBVI event. By setting these newly introduced parameters according to CFD predictions, it appears that the interaction clearly changes to an acoustically efficient dipole making these parameters important in order to assess CROR OBVI noise accurately. However, looking at the differences with numerical simulations [15], two additional features need to be investigated. First, the variation of velocity in the spanwise direction needs to be taken into account. Finally, because of the stream-tube contraction, the vortex may also impact the tip edge, questioning the present infinite span assumption and also the recently proposed correction by Roger et al. [9] that assumes a grazing vortex on the blade tip and consequently imposes a Kutta condition on the pressure locally.

Acknowledgements

Authors would like to thank Safran Aircraft Engine (SAE) for their funding through the UdeS Industrial Chair in Aeroacoustics. URANS computations were made on the supercomputer Mammouth-MP2 from Université de Sherbrooke, managed by Calcul Québec and Compute Canada. The operation of this supercomputer is funded by the Canada Foundation for Innovation (CFI), NanoQuebec, RMGA and the Fonds de recherche du Québec - Nature et technologies (FRQ-NT).

References

- [1] J.H. Dittmar, Some design philosophy for reducing the community noise of advanced counter-rotation propellers, NASA-TM-87099.
- [2] J.H. Dittmar, Cruise noise of counterrotation propeller at angle of attack in wind tunnel, NASA-TM-88869.
- [3] J.H. Dittmar, D.B. Stang, Reduction of the noise of a model counterrotation propeller at cruise by reducing the aft propeller diameter, *J. Acoust. Soc. Am.* 81 (S1) (S96–S96).
- [4] R.P. Woodward, Measured noise of a scale model high speed propeller at simulated takeoff/approach conditions, in: Proceedings of the 25th Aerospace Sciences Meeting, Reno, Nev. USA, 12–15 Jan. 1987, vol. 1, pp. 12–15, 1987.
- [5] E. Gordon, R. Woodward, Noise of a model counterrotation propeller with reduced aft rotor diameter at simulated takeoff/approach conditions (F7/A3), NASA-TM-100254.
- [6] R. Fernando, M. Leroux, Open-Rotor low speed aero-acoustics: wind tunnel characterization of an advanced blade design in isolated and installed configurations, in: Proceedings of the 20th AIAA/CEAS Aeroacoustics Conference, Atlanta, GA, USA, 16–20 June, no. 2014–2749, 2014.
- [7] L. Soulat, I. Kernemp, M. Sanjose, S. Moreau, R. Fernando, Numerical assessment of the tonal noise of Counter-Rotating Open Rotors at approach, *Int. J.*

- Aeroacoust. 15 (1–2) (2016) 23–40.
- [8] A. Peters, Z.S. Spakovszky, Rotor interaction noise in counterrotating propfan propulsion systems, *J. Turbomach.* 134 (1) (2012) 011002.
- [9] M. Roger, C. Schram, S. Moreau, On vortex-airfoil interaction noise including span-end effects, with application to open-rotor aeroacoustics, *J. Sound Vib.* 333 (1) (2014) 283–306.
- [10] L. Soulat, I. Kernemp, M. Sanjose, S. Moreau, R. Fernando, Assessment and comparison of tonal noise models for Counter-Rotating Open Rotors, in: Proceedings of the 19th AIAA/CEAS Aeroacoustics Conference, Berlin, Germany, 27–29 May, no. 2013–2201, 2013.
- [11] F. Danner, C. Kendall-Torry, H.-P. Kau, Aerodynamic origin of rotor-rotor interaction noise from unducted propulsors, in: Proceedings of the ASME Turbo Expo 2013: Turbine Technical Conference and Exposition, San Antonio, Texas, USA, June 37, 2013, American Society of Mechanical Engineers, 2013.
- [12] R. Majjigi, K. Uenishi, P. Gliebe, An investigation of counterrotating tip vortex interaction, NASA CR-185135.
- [13] M.E. Quaglia, S. Moreau, M. Roger, R. Fernando, A three-dimensional analytical approach for open-rotor blade vortex interaction (BVI) tonal noise, in: Proceedings of the 21th AIAA/CEAS Aeroacoustics Conference, Dallas, Texas, USA, 22–26 June, no. 2015–2984, 2015.
- [14] L. Vion, G. Delattre, F. Falissard, L. Jacquin, Counter-Rotating Open Rotor (CROR): flow physics and simulation, in: Proceedings of the 20ème Congrès Français de Mécanique, Besancon, France, 28 aout/2 sept.
- [15] F. Falissard, G. Delattre, Investigation of counter-rotating open-rotor orthogonal blade/vortex interaction noise, in: Proceedings of the 20th AIAA/CEAS Aeroacoustics Conference, Atlanta, GA, USA, 16–20 June, no. 2014–2748, 2014.
- [16] M.J. Kingan, R.H. Self, Counter-rotation propeller tip vortex interaction noise, in: Proceedings of the 15th AIAA/CEAS Aeroacoustics Conference, Miami, Florida, USA, 1–12 May, no. 2009–3135, 2009.
- [17] D. Fabre, *Instabilité et instationnarités dans les tourbillons: Application aux sillages d'avions* (PhD. thesis), Université Paris VI, Paris, France, 2002.
- [18] C. Oseen, Über Wirbelbewegung in einer reibenden Flüssigkeit, *Almqvist & Wiksells*, 1911.
- [19] G. Vatisstas, S. Lin, C. Kwok, Theoretical and experimental studies on vortex chamber flows, *AIAA J.* 24 (4) (1986) 635–642.
- [20] X. Carton, J. McWilliams, Barotropic and baroclinic instabilities of axisymmetric vortices in a quasigeostrophic model, *Elsevier Oceanogr. Ser.* 50 (1989) 225–244.
- [21] R.K. Amiet, High frequency thin-airfoil theory for subsonic flow, *AIAA J.* 14 (8) (1976) 1076–1082.
- [22] J. Christophe, *Application of Hybrid Methods to High Frequency Aeroacoustics* (PhD. thesis), von Karman Institute for Fluid Dynamics, Bruxelles, Belgium, 2011.
- [23] M. Roger, On broadband jet-ring interaction noise and aerofoil turbulence-interaction noise predictions, *J. Fluid Mech.* 653 (2010) 337–364.
- [24] L. Soulat, I. Kernemp, R. Fernando, Numerical assessment of noise emission of counter-rotating open rotors, in: Proceedings of the 10th European Turbomachinery Conference, Lappeerenta, Finland, 2013.
- [25] J. Caro, P. Ferrand, S. Aubert, L. Kozuch, Inlet conditions effects on tip clearance vortex in transonic compressor, in: Proceedings of the 5th European Conference on Turbomachinery Fluid Dynamics and Thermodynamics, Prague, 2003.
- [26] M.-S. Liou, A sequel to aumsm: aumsm+, *J. Comput. Phys.* 129 (2) (1996) 364–382.
- [27] J.C. Kok, Resolving the dependence on freestream values for the k-turbulence model, *AIAA J.* 38 (7) (2000) 1292–1295.
- [28] F.R. Menter, Zonal two equation k-turbulence models for aerodynamic flows, *AIAA paper* 2906 (1993), 1993.
- [29] D. Van Zante, J. Gazzaniga, D. Elliott, R. Woodward, An open rotor test case: F31/A31 historical baseline blade set, in: Proceedings of the ISABE, Gothenburg, Sweden, Aug., no. 2011–1310, 2011.
- [30] J. Jeong, F. Hussain, On the identification of a vortex, *J. fluid Mech.* 285 (1995) 69–94.
- [31] R.C. Strawn, D.N. Kenwright, J. Ahmad, Computer visualization of vortex wake systems, *AIAA J.* 37 (4) (1999) 511–512.
- [32] D.E. Van Zante, M.P. Wernet, Tip vortex and wake characteristics of a counterrotating open rotor, in: Proceedings of the 48th AIAA/ASME/SAE/ASEE Joint Propulsion Conference & Exhibit, AIAA, no. 2012–4039, 2012.
- [33] F. Gandhi, L. Tauszig, A critical evaluation of various approaches for the numerical detection of helicopter blade vortex interactions, *J. Am. Helicopter Soc.* 45 (3) (2000) 179–190.
- [34] M. Scully, *Computation of helicopter rotor wake geometry and its influence on rotor harmonic airloads* (PhD thesis), Massachusetts Institute of Technology, Cambridge, Massachusetts, USA, 1975.
- [35] G. Delattre, F. Falissard, Influence of torque ratio on counter-rotating open-rotor interaction noise, in: Proceedings of the 20th AIAA/CEAS Aeroacoustics Conference, Atlanta, GA, USA, 16–20 June, no. 2014–2969, 2014.
- [36] H. Squire, The growth of a vortex in turbulent flow, *Aeronaut. Q.* 16 (1965) 302–306.
- [37] M. Roger, S. Moreau, Back-scattering correction and further extensions of Amiet's trailing-edge noise model. Part 1: theory, *J. Sound Vib.* 286 (3) (2005) 477–506.
- [38] A. Carazo, M. Roger, M. Omais, Analytical prediction of wake-interaction noise in counter-rotation open rotors, in: Proceedings of the 17th AIAA/CEAS Aeroacoustics Conference, Portland, Oregon, USA, 5–8 June, no. 2011–2758, 2011.
- [39] I.S. Gradshteyn, I.M. Ryzhik, *Table of Integrals, Series and Products*, Academic Press, 1965.
- [40] M. Abramowitz, I.A. Stegun, *Handbook of Mathematical Functions*, Dover Publications, 1972.
- [41] S. Moreau, M. Roger, V. Jurdic, Effect of angle of attack and airfoil shape on turbulence-interaction noise, in: Proceedings of the 11th AIAA/CEAS Aeroacoustics Conference, Monterey, California, USA, 23–25 May, no. 2005–2973, 2005.
- [42] D. Zwillinger, *Table of Integrals, Series, And Products*, Elsevier, 2014.
- [43] M. Roger, A. Carazo, Blade-geometry considerations in analytical gust-airfoil interaction noise models, in: Proceedings of the 16th AIAA/CEAS Aeroacoustics Conference, Stockholm, Sweden, May, no. 2010–3799, 2010.
- [44] N. Peake, The unsteady lift on a swept blade tip, *J. Fluid Mech.* 271 (1994) 87–101.
- [45] K. Schwarzschild, Die beugung und polarisation des lichts durch einen spalt. i, *Math. Ann.* 55 (2) (1901) 177–247.
- [46] J.J. Adamczyk, Passage of a swept airfoil through an oblique gust, *J. Aircr.* 11 (5) (1974) 281–287.
- [47] S. Moreau, M. Roger, Competing broadband noise mechanisms in low-speed axial fans, *AIAA J.* 45 (1) (2007) 48–57.
- [48] F. Coton, J. Marshall, R. Galbraith, R. Green, Helicopter tail rotor orthogonal blade vortex interaction, *Progress. Aerosp. Sci.* 40 (7) (2004) 453–486.
- [49] N. Curle, The influence of solid boundaries upon aerodynamic sound, in: Proceedings of the Royal Society of London. Series A. mathematical and Physical Sciences, 231 (1187), 1955, pp. 505–514.
- [50] X. Liu, J. Marshall, Blade penetration into a vortex core with and without axial core flow, *J. Fluid Mech.* 519 (2004) 81–103.